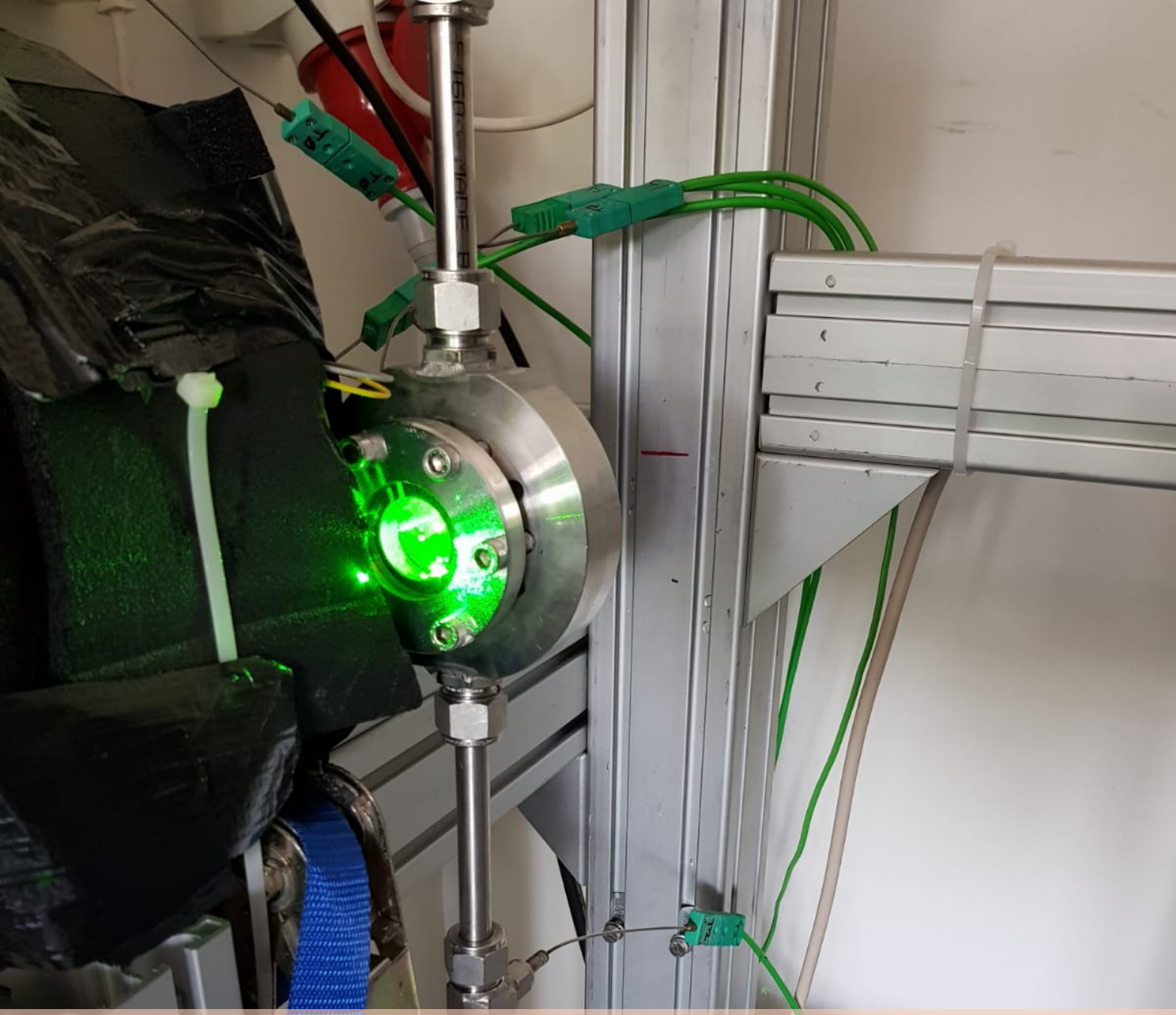

Feasibility study on Laser Doppler Anemometry in Supercritical Fluids

Leon de Vries - Delft University of Technology

Supervisor:

Dr. Martin Rohde

Committee Members:

Dr. Martin Rohde, Dr. Danny Lathouwers, Dr. Jurriaan Peeters

This page is intentionally left blank.

Abstract

A feasibility study was performed for seeding particles in a supercritical environment with a two component Laser Doppler Anemometry (LDA) system. The seeding particles were different in their density, four different seeding particles were tested: 1.00 g/ml, 0.79 g/ml, 0.55 g/ml and 0.36 g/ml. Furthermore, the applicability of LDA in an environment with a steep density gradient was tested as the refractive index changes with the changing density. This study uses Trifluoromethane or Freon-23, abbreviated as freon as supercritical fluid. The fluid flows in mixed convection through the setup, which allows the measurement of two velocity components in the measurement volume: a orthogonal cylinder ($L = 25$ mm, $R = 10$ mm) with a glass window at the front and a copper backside. The copper backside has a heating element embedded in it to apply a heat flux for the density gradient measurements. Several locations were probed to measure the velocity at different inlet temperatures. The centerline, the depthline and both the inlet and the outlet provide valuable information on the performance of the seeding types. The performance of the seeding types is determined by a comparison with FLUENT simulated data and the turbulent free jet approach. The results show discrepancies between the simulations and the experimental measurements. Both the amplitude and the velocity profile do not match in nearly all cases that were studied. This raised the believe that the simulation seem to contain errors as the experimental results show agreement with reference velocities calculated from values from the setup. The results of the density gradient measurements with local heating show a velocity amplitude decrease in 4 of the 6 measurements. This decrease appears to be the result of the large density difference and the resulting bouyancy effects and refractive index changes.

Contents

Pretty fluids, ©No idea

1. Introduction

Pretty fluids, ©No idea

The supercritical water reactor (SCWR) has been selected as one of the promising next steps in nuclear reactor design [1]. This gen IV reactor type is an improvement on the light water reactor (LWR). The differences are the operating pressure (250 bar) and the increased exit temperature (510°C). These differences are presented to increase the thermal efficiency from 33% to 44% without applying radically new technological advancements but instead building upon the established and well-known LWR's and supercritical fossil plants. An important factor in a reactor is the heat transfer from the irradiated core to the coolant, which passes through a turbine to generate electrity. An increased specific heat (c_p) would indicate the same energy transport at a lower thermal difference. The supercritical fluid remains a single phase but has significant changes in its thermophysical properties as it loops around the reactor and the turbine. In the past 60 years, a significant amount of research on the heat transfer to supercritical fluids has been carried out. This was summarized by Pioro et al. [2].

As nuclear reactors or supercritical fossil plants are costly builds, a detailed analysis on the flow of the supercritical fluid is necessary to reduce operating costs and to know its properties. To measure this flow, several methods are available in literature, as described by Adrian (1991) [3]. Some notable methods are the hot wire anemometry (HWA), the particle image velocimetry (PIV) and the laser doppler anemometry (LDA). But where HWA, as used by Taeger (1980) [4], for example, uses a wire inside the fluid flow, therefore affecting the flow itself, the other methods are used from outside the flow, see Deen et al. (2000) [5]. Both PIV and PDA use lasers to measure the velocity in two fundamentally different ways, but need particles inside the fluid to make the fluid visible for the lasers of the system. PIV, as used by Valori (2018) [6] for example, uses a laser sheet emitted at two times with a known short time interval to calculate the velocities of the particles, whereas LDA, as used by Jackson (2006) [7], uses the the doppler shift of the reflections of the particles to calculate the velocities, as explained by Scarano (2013) [8]. The lasers of both systems do not affect the flow direction as the photon momentum is negligible for commonly used laser powers. The particles, also known as seeding particles or tracer particles, have to accomodate for different properties to be able to follow the fluid without obstructing it and therefore determine the quality of the measured data.

Feasability studies have been carried out on seeding particles for PIV [9, 10], and on seeding particles in supercritical fluids [6], but few studies have been done on seeding particles in supercritical flow measurement using a Laser Doppler Anemometry system [1]. Therefore the goal of this study is to indicate the effects of the temperature, the pressure and the density of the seeding particles on the velocity profile of a supercritical flow through a orthogonal cylinder. There was little funding for this study, hence the orthogonal cylinder is chosen as it was a leftover from another setup and the name is chosen as SCR00G€, which stands for SuperCRitical facility with 00 Giga

€uros. In this study the name will be abbreviated to Scrooge.

This study will try to answer the following research questions:

- What is the velocity profile after performing LDA on a supercritical fluid?
- What is the effect on the velocity profile when using different seeding types while performing LDA on a supercritical fluid?
- Which seeding type is the most accurate in describing the fluid flow?
- What is the effect on the velocity profile when heating the backside of the measurement volume?

These questions will be answered via experimental measurements, which will be compared to simulations. The simulations will be done in ANSYS FLUENT [11]. The experimental measurements will be done in different cases with different inlet temperatures. The inlet temperature is measured in the inlet tube 10 cm before the measurement volume as the thermocouple is located there. The velocity profile will be measured on different locations and at different inlet temperatures. The velocity profiles will be measured for different seeding particles to indicate their effects on the measured flow.

2. Theory

Bubbles and Waves ©Ice River Springs [12]

In this chapter the theory that is used will be explained. Starting with the supercritical fluids in section 2.1, followed by the supercritical fluid that is used in this study, freon, in section 2.2. A measure for the results will be introduced in section 2.3: the turbulent free jet approach as well as a way to obtain the results in section 2.4, namely, the Laser Doppler Anemometry system.

2.1 Supercritical Fluids

Materials can exist in many different phases. Some of these phases like the solid phase, the liquid phase and the gaseous phase are well-known as these states exist at room temperature and atmospheric pressure for almost all materials. However, the further away from this temperature and pressure, other phases exists. The triple point is a single point where the material coexists in solid, liquid and gaseous phase at the same time.

Next to the gaseous, fluid and solid phases, a fourth phase is the supercritical fluid phase. This phase exists at pressures and temperatures above the critical point as seen in figure 2.1. These supercritical fluids are a combination of the gaseous phase and the liquid phase, but without an interface between them. This means that the fluid has both gas-like properties and fluid-like properties. The ratio between these properties depends on the pressure and the temperature: an increase in temperature makes supercritical fluid properties more gas-like and an increase in pressure makes them more fluid-like.

The critical point is different for each different material and it is characterized by its critical temperature T_c and critical pressure P_c. These parameters are tabled for several different materials in table 2.1. Water has a relatively high critical pressure and temperature at $T_c = 374.14$ °C or 647.3 K and $P_c = 220.9$ bar [13] and therefore is hard to use in experimental areas due to the high pressure and temperature demands. This is why freon-23 is used in this study, see section 2.2.

2.1.1 Supercritical Properties

Materials have certain properties which are most of the time considered constant, such as density, viscosity and specific heat. These properties are in fact not constant over different temperature and pressure ranges, but change constantly when the temperature or pressure is changed. When the pressure and the temperature approach their critical levels, these properties start to change heavily. The changes are plotted in figure 2.2. The density ρ, thermal conductivity λ and the dynamic viscosity μ all make a steep decrease in value, whereas the thermal diffusivity α has a small dip after which it increases a lot, the kinematic viscosity ν increases significantly after the critical temperature and the specific heat c_p, Reynolds number Re and Prandtl number Pr spike around the critical temperature.

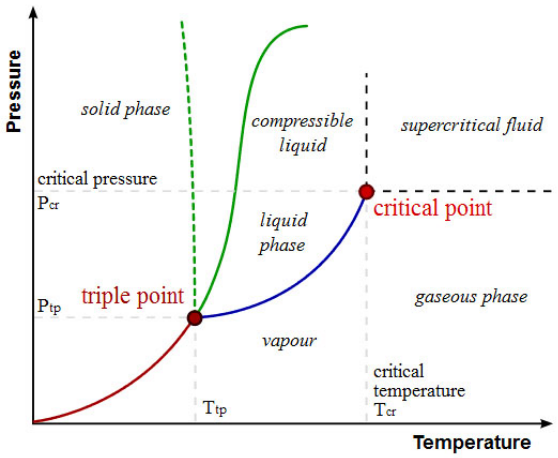

Figure 2.1: Pressure-Temperature diagram depicting the several phases in which a material can exist. The dotted lines right and above the critical point indicate that no difference can be seen between the phases [14].

Table 2.1: Several commonly studied materials with their respective critical temperature T_c and critical pressure P_c [15]. The critical pressure and temperature of water are much higher than those of freon, making it easier to create supercriticial freon. Table extended from Samadzadeh (2019) [16].

Material	Critical Temperature (K)	Critical Pressure (bar)
Hydrogen (H)	33.3	13.0
Neon (Ne)	44.4	26.6
Nitrogen (N)	126	33.9
Argon (Ar)	151	49.1
Methane (CH_4)	191	46.4
Ethane (C_2H_6)	305	48.8
Carbon Dioxide (CO_2)	305	73.9
Ammonia (NH_3)	406	113
Water (H_2O)	647	221
Freon-23 (CHF_3)	299	48.3

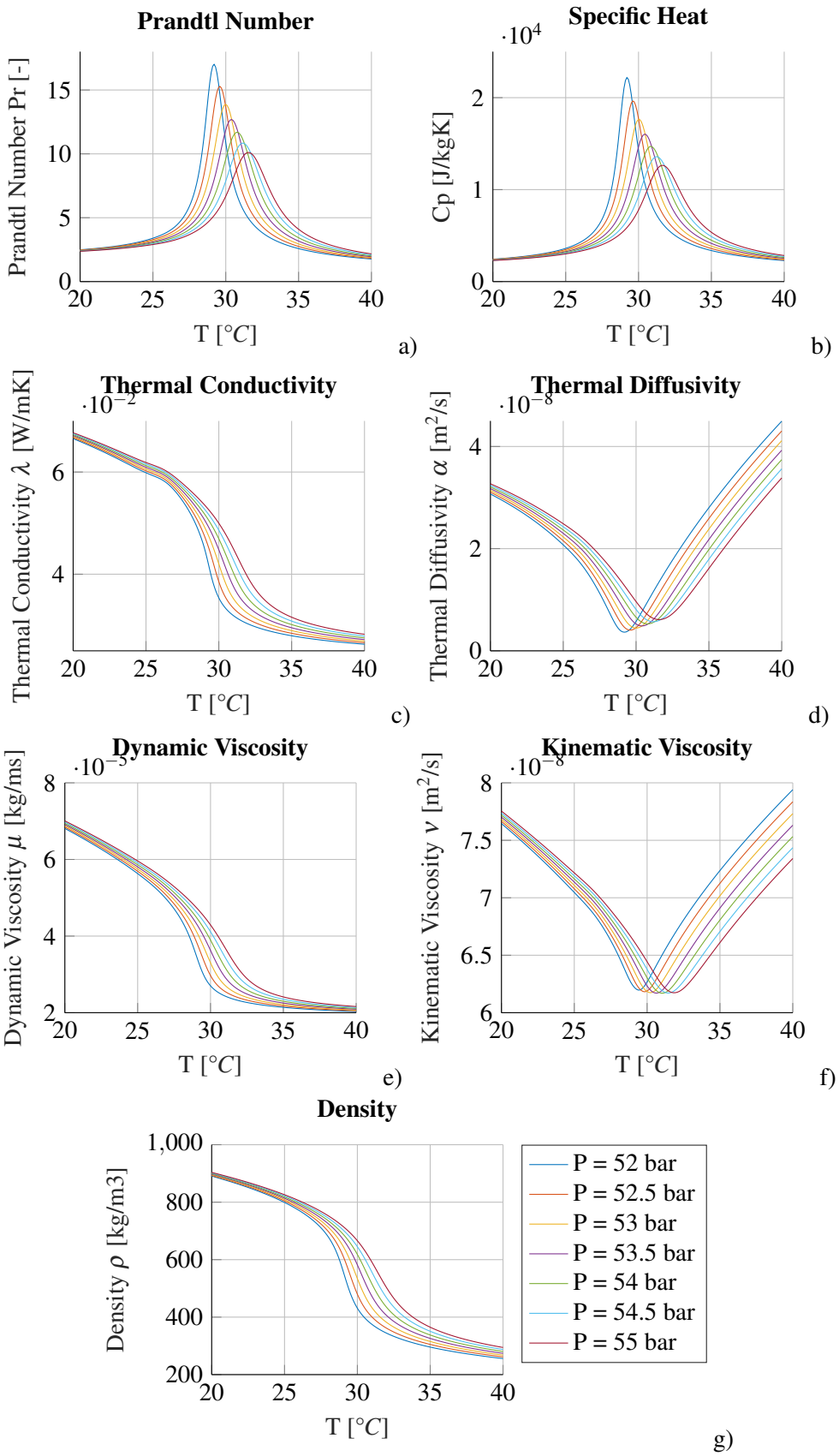

Figure 2.2: The Prandtl number $Pr = \frac{\nu}{\alpha}$ is shown in a), the specific heat c_p in b), the thermal conductivity λ in c), the thermal diffusivity $\alpha = \frac{\lambda}{\rho c_p}$ in d), the dynamic viscosity μ in e), the kinematic viscosity $\nu = \frac{\mu}{\rho}$ in f) and the density ρ in g). Images created using MATLAB (2017) with data from the coolprop database (2019) [17, 18].

2.1.2 Supercritical Heat Transfer

As introduced in chapter 1, Pioro et al. [2] summarized the past 60 years of research on heat transfer in supercritical fluids. This was needed as experiments have shown that variable property fluids can cause an enhancement or a deterioration in heat transfer [19]. For example, at relatively low mass velocities, bouyancy effects are important due to density gradients in the fluid. The heat transfer can therefore result in deterioration or enhancement depending on the flow direction [20]. Downwards flow enhances the heat transfer, where upwards flow deteriorates the heat transfer [21]. At relatively high mass velocities, the bouyancy effects become unimportant and the flow is considered to be in forced convection [22]. Many Nusselt correlations are presented, but not many are able to accomodate and predict the deterioration and enhancement effect [23]. Some other effects are the very effective heat transfer in the near-critical region with low heat flux, reduced effectiveness of heat transfer with increase of heat flux and seriously impaired heat transfer with strong heating [24].

2.2 Freon-23

Freon-23, also known as R-23, HFC-23 or abbreviated as freon in this study, is a trihalomethane, which is a methane molecule (CH_4) with three halogen atoms replacing three hydrogen atoms. R-23 replaces the hydrogen atoms with three fluor atoms, making it a Haloform with the chemical formula CHF_3 [25]. It has a much lower critical temperature and pressure than water, namely $T_c = 25.92$ °C and $P_c = 48.36$ bar [26]. Freon is created mainly as a by-product in the production of Teflon and therefore is widely available [27]. It can also be created organically via decarboxylation of trifluoroacetic acid in small amounts [28].

Near the critical point another widely used set of points exist: the pseudo-critical points (T_{pc}, p_{pc}). These points are defined as the temperatures $(T_{pc} > T_c)$ where the specific heat is at its maximum. The other properties undergo the most heavily changes at these points, this is shown in figure 2.2 [29].

2.3 Turbulent Free Jet

The flow inside the measurement volume is too complex to be analyzed analytically. Therefore the flow will be approached from the turbulent free jet view. As the first part of the jet flowing into the window has no obstructions from the walls, the free jet approach should provide a basic insight in the flow.

In contrary to what is expected from a supercritical fluid, the free jet approach assumes a constant density over the whole jet. Besides, it is generally assumed that there are zero wall effects. Nieuwstadt et al. (2016) (p.120) [30] said: "In general the effects of walls can be ignored when the cross section of external domain is at least 10^5 times the cross section $\frac{1}{4}\pi d^2$ of the nozzle." Here d is the diameter of the nozzle. The inlet nozzle of the setup is $A_{inlet} = 0.79\text{cm}^2$, which concludes that the cross section of the window should be at least 7.5 m^2, which is about 1.6×10^4 times larger than the maximum cross section of the window ($A_{window,max} = 0.025 * 0.02\text{m}^2 = 5.0\text{cm}^2$). Therefore it is highly unlikely that the free jet approach will give accurate results in a geometry which does not allow the same conditions. It can only be used as a reference for the results.

In Nieuwstadt et al. (2016) [30], expressions for the mean velocities $\overline{u}$ and $\overline{v}$ are found. Here, $\overline{u}$ represents the mean velocity in the flow direction and $\overline{v}$ the mean velocity in the radial direction.

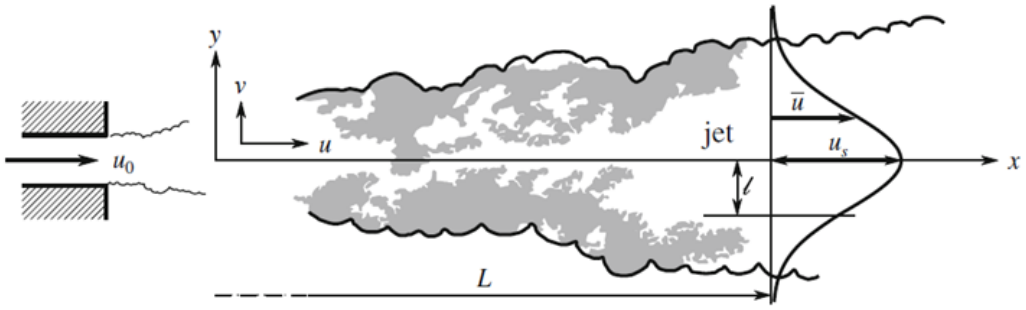

Figure 2.3: Overview of the used variables and directions in section 2.3. After: Tennekes and Lumley (1972). See Nieuwstadt et al. (2016) figure 6.15 [30, 31].

The expressions for $\bar{u}$ and $\bar{v}$ are shown in equations 2.1-2.2.

$$\bar{u} = u_s \left(1 + \frac{\eta^2}{8B}\right)^{-2} \tag{2.1}$$

$$\bar{v} = u_s \frac{dl}{dx}\left(\frac{4B\eta(8B-\eta^2)}{(8B+\eta^2)^2}\right) \tag{2.2}$$

With $\eta = r/l(x)$, $l = 0.0965(x - x_0)$ and $B = 0.302$. The expression for l was confirmed by Fukushima et al. (2002) [32] by using K-theory [33]. The mean velocities $\bar{u}$ and $\bar{v}$ are dependent on the spatial location and a reference velocity u_s only.

2.3.1 Inlet velocity

An expression is found for the mean velocities $\bar{u}$ and $\bar{v}$ which is dependent on the reference velocity u_s. To know the velocity $\bar{u}$ itself, a value for u_s is needed. This is calculated using the equation for the massflow:

$$\dot{m} = \rho v_{avg} A_{inlet} \tag{2.3}$$

Here v_{avg} is the averaged velocity averaged in time and over the inlet area A_{inlet}. ρ is the density at the inlet, which is taken as the density corresponding with the pressure and temperature according to the Thermophysical Property Database Coolprop and the NIST Database [18, 34].

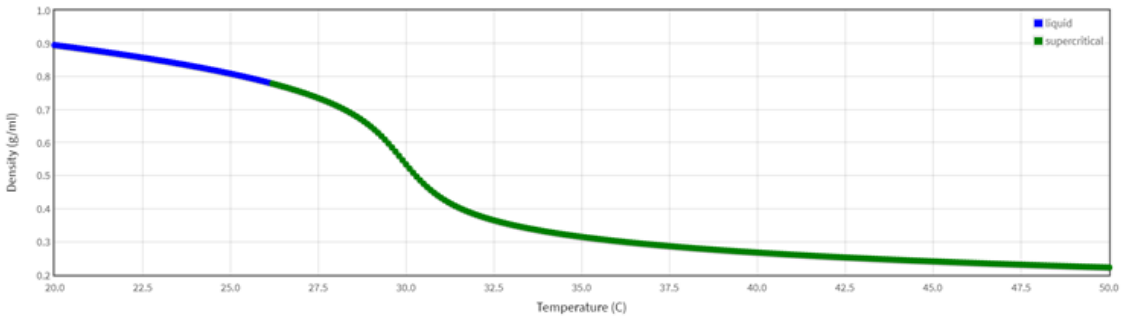

Figure 2.4: The density of freon for different temperatures at a constant pressure of $P = 53$ bar. Data aquired from the NIST database [34].

By measuring the freon massflow in the setup with the Coriolis meter and using the density from figure 2.4, the average velocity can be calculated. This average velocity will be used as the reference

velocity u_s to calculate the mean velocities $\overline{u}$ and $\overline{v}$. Therefore:

$$u_s = v_{avg} = \frac{\dot{m}}{\rho A} \tag{2.4}$$

The inlet temperature T_{in}, the corresponding inlet density ρ and the calculated u_s are listed in table 2.2.

Table 2.2: Table with the used inlet temperatures. The density is evaluated at a constant pressure $P = 53$ bar using the NIST database [34].

T_{in}	ρ	u_s
27°C	0.750 g/ml	33.95 m/s
29.5°C	0.600 g/ml	42.44 m/s
30.3°C	0.500 g/ml	50.93 m/s
33°C	0.350 g/ml	72.76 m/s

2.4 Laser Doppler Anemometry System

The Laser Doppler Anemometry system (LDA system), also known as a Laser Doppler Velocimetry system (LDV system), uses two sets of two lasers, one pair horizontally and one pair vertically placed, to measure the Doppler shift of the reflection from particles flowing through the loop of the Scrooge. The workings of an LDA system will be explained in this section.

2.4.1 Doppler Shift of a Single Beam

The Laser Doppler Anemometry system is, as the name suggests, a system that performs measurements of the Doppler shift using lasers. The Doppler shift is created because the light of a moving particle with velocity $\vec{U}$ scatters the light from the lasers with wavelength λ_0 and frequency f_0. The laser is pointed in the direction of unit vector $\vec{l}_i$ as seen in figure 2.5.

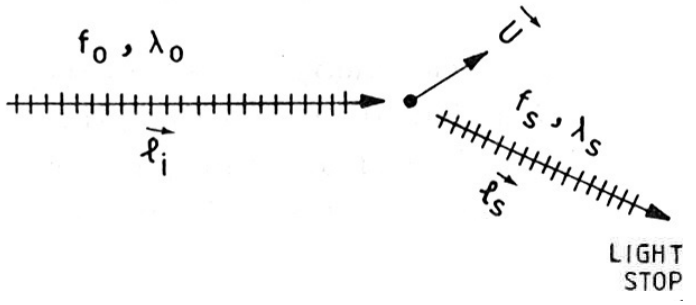

Figure 2.5: A light wave (f_0, λ_0) hits a moving particle with speed $\vec{U}$ and scatters as a wave with f_s, λ_s. This setup is set in Reference beam mode, see section 2.4.2. Figure from [8].

The light will be scattered in all directions, but let's take for example the direction of unit vector $\vec{l}_s$. This wave will have a frequency f_s and wavelength λ_s. This results in a Doppler shift of $f_D = f_0 - f_s$. The wavefronts of both waves will have a relative speed of $\lambda_0 f_0 - \vec{U} \cdot \vec{l}_i$ and these wavefronts will be intercepted by the moving particle at a rate of f'.

$$f' = \frac{\lambda_0 f_0 - \vec{U} \cdot \vec{l}_i}{\lambda_0} = f_0 - \frac{\vec{U} \cdot \vec{l}_i}{\lambda_0} \tag{2.5}$$

With $\lambda_0 f_0 = c$ with c equals the speed of light in the medium the laser propagates. An observer that only observes the wavefronts of the scattered wave, observes the wavefronts at a rate of f_s.

$$\begin{aligned} f_s &= \frac{\lambda_0 f_0 + \vec{U}\cdot\vec{l_s}}{\lambda_s} \\ &= f' + \frac{\vec{U}\cdot\vec{l_s}}{\lambda_s} \\ &= f_0 + \vec{U}\left(\frac{\vec{l_s}}{\lambda_s} - \frac{\vec{l_0}}{\lambda_0}\right) \end{aligned} \tag{2.6}$$

Because the Doppler shift frequency $F_D \sim 10^6$ Hz is much lower than the frequency of the lasers, $f_0 \sim 10^{14}$ Hz, the assumption $f_0 \approx f_s$ can be taken. This means that:

$$f_s = f_0 + \frac{\vec{U}}{\lambda_0}(\vec{l_s} - \vec{l_i}) \tag{2.7}$$

$$f_D = f_s - f_0 = \frac{\vec{U}}{\lambda_0}(\vec{l_s} - \vec{l_i}) \tag{2.8}$$

Therefore, the Doppler shift is related to the velocity of the moving particle and also the directions of the particle and the incoming and scattered lasers.

2.4.2 Two Beam Modes

The Doppler shift is used in the LDA with a combination of two lasers. The LDA can be used in two modes containing two laser beams: The reference beam mode and the crossbeam mode.

Reference Beam Mode

Two beams with a different intensity illuminate a single particle. The low intensity reference beam is used to determine the Doppler shift as seen in figure 2.6. Here the incoming lasers with frequency f_0, wavelength λ_0 and direction vector $\vec{l_{i1}}$ and $\vec{l_{i2}}$ arrive at a particle with velocity $\vec{U}$. A photodetector is aligned with the low intensity beam. The light scattered from the interaction with the high intensity beam will be combined with the light directly passing of the low intensity beam. At the photodetector the total electric field vector is given by:

$$E_t = E_1 \cos(\omega_1 t) + E_{2'} \cos(\omega_2 t) \tag{2.9}$$

Here E_1 and E_2 [V/m] are the amplitudes of the transmitted and scattered light intensity respectively. The photodetector has a response that is proportional with the square of the electric field:

$$E_t^2 = E_1^2 \cos^2(\omega_1 t) + E_{2'}^2 \cos^2(\omega_2 t) + E_1 E_{2'} \cos((\omega_1 + \omega_2)t) + E_1 E_{2'} \cos((\omega_1 - \omega_2)t) \tag{2.10}$$

The photodetector is not able to respond to the electrical field variations at frequencies ω_1 or ω_2, which are of the order of $\sim 10^{14}$ Hz. Therefore only the average value of the electrical field is returned for the first three terms. These three average terms are $\frac{1}{2}E_1^2$, $\frac{1}{2}E_2^2$ and 0, respectively. The respons of the detector is given by:

$$E_D^2 = \frac{E_1^2}{2} + \frac{E_{2'}^2}{2} + E_1 E_{2'} \cos((\omega_1 - \omega_2)t) \tag{2.11}$$

Discarding the DC output terms and keeping the fluctuating terms, combining with the fact that the Doppler shift is the difference between the transmitted and scattered frequency like $f_D = f_{2'} - f_0$, using $f_1 = f_0$ for the reference beam as shown in figure 2.6, the outcome is [8]:

$$E_D^2 = E_1 E_{2'} \cos(2\pi f_D t) \tag{2.12}$$

which is easier to measure. However, this method requires the scattered beam to be in the same direction as the transmitted beam and therefore only a small solid angle can be measured, which gives a low data rate and to avoid a broadening of the frequency spectrum as the frequencies are nearly the same anymore at larger angles.

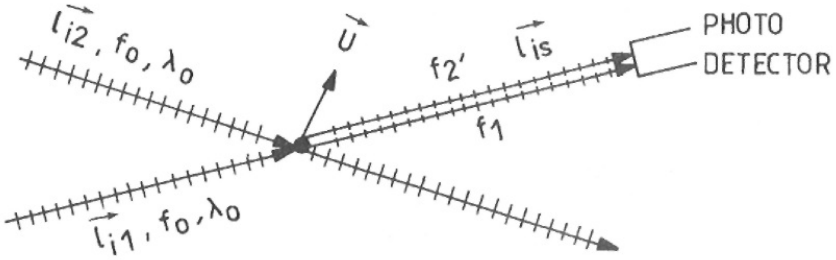

Figure 2.6: Reference Beam Mode. The incoming lasers with frequency f_0, wavelength λ_0 and direction vector $\vec{l_{i1}}$ and $\vec{l_{i2}}$ arrive at a particle with velocity $\vec{U}$ and generate the scattered wave with $f_{2'}$ and $\vec{l_{is}}$. Figure from [8].

Crossbeam Mode

Another way of using the lasers is the crossbeam mode from figure 2.7. This way both lasers are scattered to (f_{s1}, λ_{s1}) and (f_{s2}, λ_{s2}) along direction $\vec{l_s}$ for instance. According to Scarano [8] the Doppler frequency can be calculated with:

$$f_D = f_s - f_0 = \frac{\vec{U}}{\lambda_0}(\vec{l_s} - \vec{l_i}) \tag{2.13}$$

The scattered beams have the frequencies:

$$f_{s1} = f_0 + \frac{\vec{U}}{\lambda_0}(\vec{l_s} - \vec{l_{i1}}) \tag{2.14}$$

$$f_{s2} = f_0 + \frac{\vec{U}}{\lambda_0}(\vec{l_s} - \vec{l_{i2}}) \tag{2.15}$$

And these can be combined to form the equation for the Doppler frequency, which is:

$$f_D = f_{s2} - f_{s1} + \frac{\vec{U}}{\lambda_0}(\vec{l_{i1}} - \vec{l_{i2}}) \tag{2.16}$$

And this frequency can be detected at the photodetector. As in the reference beam mode the photodetector is not able to measure the high frequencies and therefore only measures the difference between the frequencies of the two beams. However, the benefit of this method is the lack of dependency on the angle between the scattered light. As long as the light is directed towards the surface of the detector, the light can be collected from a more wide solid angle than with the Reference Beam Mode.

Added effect of the crossbeam mode is the creation of fringes at the intersection as seen in figure 2.8. These interference fringes arise from the two laser beam with equal intensity and create a pattern of bright (constructive interference) and dark fringes (destructive interference). When a particle moves through the intersection area, it will move through the different fringes, but only when the particle moves through the bright fringes, there is light to reflect to the detector. This

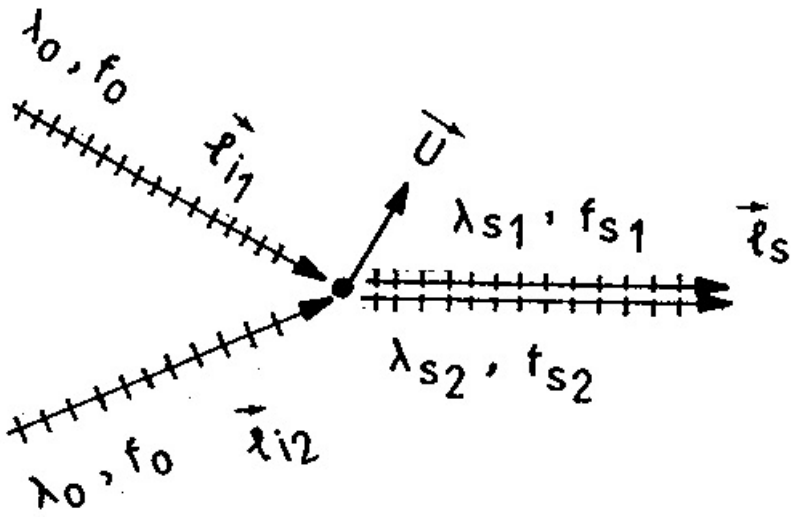

Figure 2.7: Crossbeam Mode. Both incoming lasers with λ_0 and f_0 (directions $\vec{l}_{i1}$ and $\vec{l}_{i2}$) are scattered to (f_{s1}, λ_{s1}) and (f_{s2}, λ_{s2}) along for instance the direction $\vec{l}_s$ due to a particle with a velocity $\vec{U}$. Figure from [8].

means that a oscillating pattern will be formed which has a much lower frequency than the lasers itself. This results in a smaller measurement volume and therefore a more accurate measurement. The spacing between the fringes is predicted by:

$$d_f = \frac{\lambda}{2\sin(\theta/2)} \tag{2.17}$$

With λ the wavelength of the lasers and θ the angle between them.

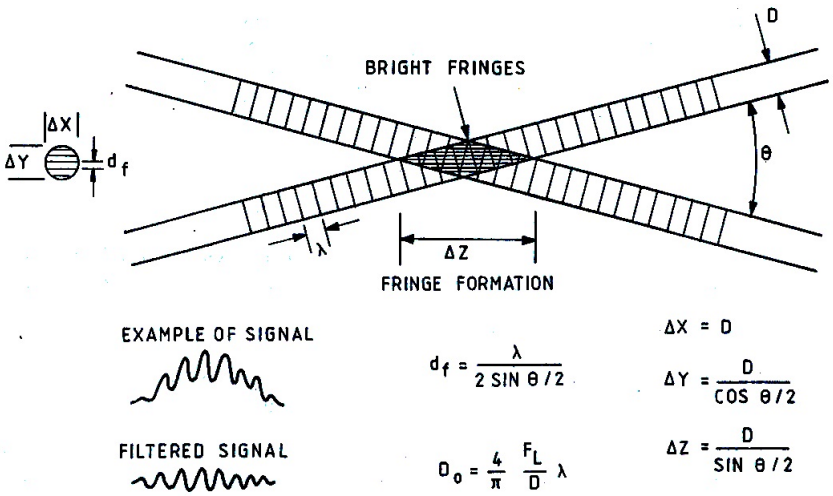

Figure 2.8: Fringes created when in crossbeam mode. The fringes occur due to interference effects and are created in a pattern of bright and dark fringes with a spacing d_f according to equation 2.17. Figure from [8].

2.4.3 Optical Configuration

The configurations for both modes are sketched in figure 2.9. To create a good spatial resolution, the measurement volume must be as small as possible. In both modes the measurement volume

is located at the intersection of the lasers. So smaller, more focused lasers create a smaller measurement volume, which in turn gives a better spatial resolution. This volume parameters Δx, Δy and Δz are calculated as seen in figure 2.8 via the waist diameter D_0.

$$D_0 = \frac{4F_L}{\pi D}\lambda \tag{2.18}$$

$$\Delta x = D_0 \tag{2.19}$$

$$\Delta y = \frac{D_0}{\cos(\theta/2)} \tag{2.20}$$

$$\Delta z = \frac{D_0}{\sin(\theta/2)} \tag{2.21}$$

Where F_L is the focal length of the lens and D the diameter of the beam.

Both modes have several components in common: a laser, illuminating optics, light stops, receiving optics and a photodetector. The illuminating optics also include a beamsplitter to create two coherent laser beams and a lens system to guide the lasers towards the wanted measurement volume. The receiving optics collect the scattered light and guide it towards the detector. In reference beam mode the receiving optics consist of only two light stops to create a small solid angle and shielding from the rest of the radiation. In crossbeam mode the light is collected by a lens or a wide solid angle and guided towards the detector. A light stop is placed to prevent outside light to enter the detector.

The differences can be found in the signal intensity and practical convenience. The intensity of the reference beam mode is much lower since the angle of collection is much smaller as opposed to the crossbeam mode, which uses a large angle to collect the scattered light. The reference beam mode needs to have the receiving optics at the opposite side of the measurement volume from the illuminating optics, since one of the lasers is transmitted. The crossbeam mode has no such restriction and therefore the illuminating optics and the receiving optics can be placed on the same side and therefore placed on a single stand to move the whole instrument at once. Also the backside of the measurement volume is not needed for the measuments, which makes crossbeam more convenient to use in tight experimental spaces as the Scrooge setup. The backside of the tube window of the Scrooge setup is made of copper and used to heat the fluid inside and therefore is not transparent for lasers, which makes the crossbeam mode necessary to use in this experiment.

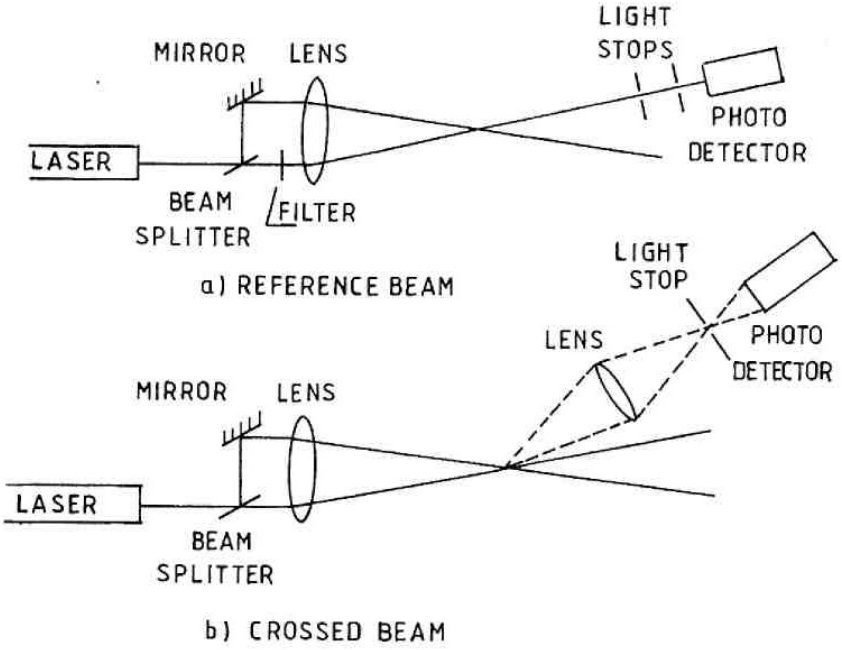

Figure 2.9: Configurations of both modes. Figure from [8].

3. Experimental Setup

Splash ©BRB [35]

Laser Doppler Anemometry is done to visualize the flow through a setup by using lasers to measure the Doppler frequency. The flow is measured in a setup called the SCR00G€ setup, which is a set of loops filled with refrigerant R23, also known as Freon-23, but abbreviated to freon in this study [26].

3.1 Scrooge Setup

The setup used to measure the velocity field is the Scrooge Setup. Preliminary measurements were done in the Scrooge 3.0 experimental facility. To accomodate other experiments in the same facility, the facility was reconfigurated to the Scrooge 6.0 experimental facility.

3.1.1 Scrooge 3.0

Preliminary measurements were done with the Scrooge 3.0 setup as shown in figure 3.1. The loop is built to measure two components of the velocity field of a flow in natural, forced or mixed convection. Natural convection can be created using the 100 cm long heated rod at the bottom tube of the main loop and a heat exchanger at the top tube to create a thermodynamic instability. Forced convection can be achieved with the pump before the heated rod in the bottom tube. This, however, does not mean that the flow through the measurement volume is considered the same convection as the entire loop, as shown in section 3.1.2.

The velocity field of freon will be measured when freon has achieved a supercritical state. To create this state, the freon is put under high pressure, above its critical pressure, and is heated above its critical temperature. The velocity field will be measured in the measurement volume, also denoted as the tube window or window. This measurement volume is a orthogonal cylinder in the tube with dimensions $R_{window} = 10$ mm and $L_{window} = 25$ mm.

Measurement Volume

The measurement volume or tube window is a cylinder in the loop with its flat surface pointed towards the LDA system. The front is transparent for optical light so the LDA lasers can reach the flow. The back of the window is made of a copper cylinder with three built-in thermocouples (T6-T8) and a heating section which is connected to a Delta SM300-20 (300V, 20A) power supply. The middle of the the main loop with $R_{tube} = 5$mm is connected to the window in the middle. The window can be seen in figures 3.2 and 3.3.

To measure the velocity field of the freon, it will flow through the loop in the clockwise direction. This motion is generated by heating and cooling the freon. The freon is heated via the heating rod

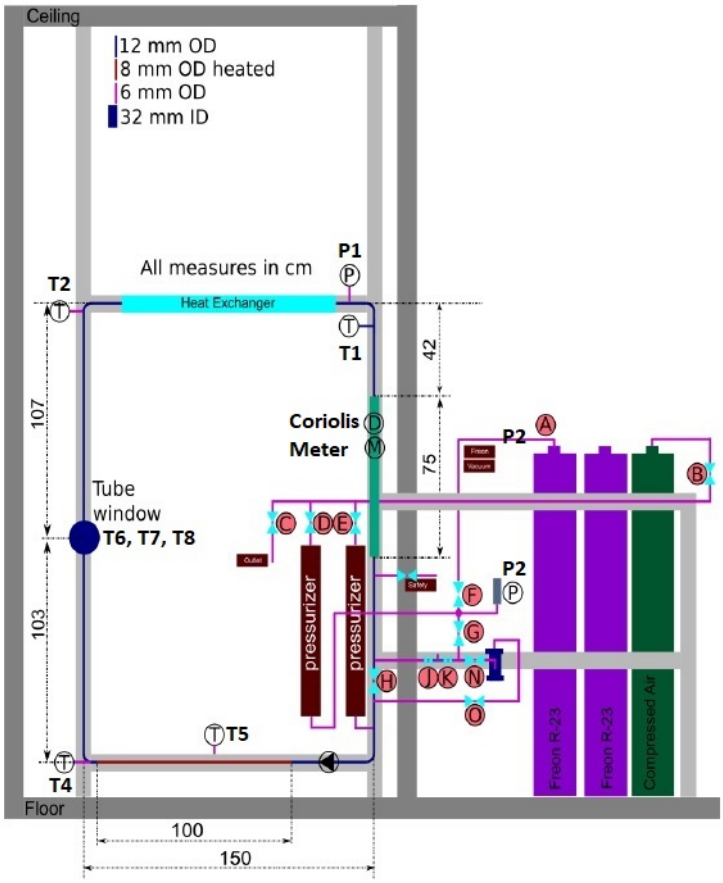

Figure 3.1: The Scrooge 3.0 setup. The setup contains a heating tube on the down side, a measurement volume called the Tube Window, a heat exchanger to cool the freon, a pump to cause forced convection, several thermocouples to measure the temperature (T) which are listed in table 3.1, a Coriolis meter to measure the average velocity and density of the Freon (green D, M), two pressure meters to measure the pressure (P), a system to insert the seeding inside the loop (valves G,H,J,K,N,O) and a system to empty or fill the whole system with Freon or compressed air using pistons/pressurizers and external tanks (tank A and valves B-F). [36]

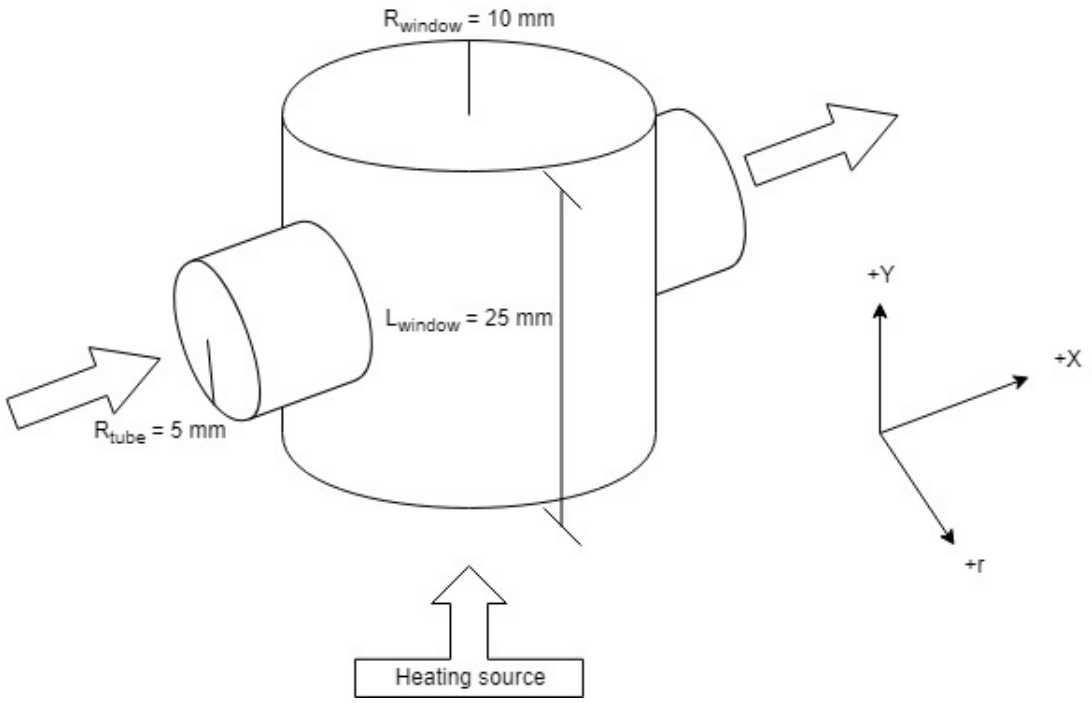

Figure 3.2: The measurement volume is an orthogonal cylinder embedded in the loop on the left side, which is shown in figure 3.1. The cylinder has a radius $R_{window} = 10$ mm and a length $L_{window} = 25$ mm. The cylinder is connected to the inlet tube and the outlet tube on opposite sites ($R_{tube} = 5$ mm). The positive x-direction is taken in the flow direction as shown by the open arrows. The copper backside can be heated and contains three thermocouples to measure the temperature. This is indicated by the lower open arrow called 'Heating Source'.

in the bottom tube of the loop or via the copper heating element inside the window. It is cooled down by a heat exchanger coupled to the cooling water system.

3.1.2 Natural, Forced or Mixed Convection

The experimental setup consists of a loop, which is built to measure two components of the velocity field of a flow in natural, forced or mixed convection. The loop can be in a form of convection, but the measurement volume does not have to be in the same form of convection. This is regulated by the bouyancy criterion, which is an analytical method developed by Jackson et al. [20]. This method identifies if the data is influenced by bouyancy. The identifying is done via the dimensionless number $Gr/Re^{2.7}$, which uses the Grashoff Number and the Reynolds Number:

$$Gr = \frac{g\beta(T_s - T_\infty)L^3}{\nu^2} \tag{3.1}$$

$$Re = \frac{\rho u L}{\mu} \tag{3.2}$$

Here, g is the acceleration due to Earth's gravity, β the thermal expansion coefficient, T_s the surface temperature, T_∞ the bulk temperature, L the length scale, ν the kinematic viscosity, ρ the density, u the velocity and μ the dynamic viscosity. For the entire loop, $L = 2$ m, but for the measurement volume, $L = 2 \times 10^{-2}$ m. At $Gr/Re^{2.7} < 10^{-5}$, the data are in the forced convection region, at $Gr/Re^{2.7} > 10^{-5}$, the data are in the mixed convection region [19].

For the thermal expansion, $1/T$ will be used as an approximation. The bulk temperature T_∞ will be set to the inlet temperature T_{in}. The surface temperature will be set to the average of the local varying temperatures T_L, which will be further explained in section 5.5. Therefore, the bouyancy criterion $Gr/Re^{2.7} = 67.3$ for the entire loop and $Gr/Re^{2.7} = 6.73 \times 10^{-5}$ for the measurement volume, which means that both the entire loop and the measurement volume are in the mixed convection region.

3.1.3 Control Systems and Sensors

Several systems and sensors regulate this flow and allow for control over the flow. Eight thermocouples and two pressure sensors measure the average temperature and average pressure of the flow, respectively, at their points in the loop. A Coriolis meter measures the average density and the massflow $\dot{m}$ through the loop and is located at the right side of the loop above the secondary loop connections. At the lower right side the connections to the secondary loop are located. This loop is used to insert the seeding particles and to increase/decrease the pressure inside the setup. The loop can be divided into several parts: The bottom tube with the heated rod and the pump, the rising tube with the window, the top tube with the heat exchanger, the descending tube with the Coriolis meter and finally the connections to the secondary loop with the pressure regulations and filling facilities [36].

Sensors

Several sensors are embedded in the loop at several locations. The pressure sensors and thermocouples are built in via T-pieces. The Coriolis meter is placed in line with the main loop.

1. **Coriolis Meter**: The ABB FCM2000 Coriolis mass flowmeter is located in the right section of the loop as shown in figure 3.1. It measures the flow through the loop, but also the average density and temperature.
2. **Absolute Pressure Measurement**: The absolute pressure is measured using a Siemens Sitrans Series Z 0-100 bar. The sensor (P1) is located in the top right corner after the heat exchanger, see figure 3.1. A second sensor (P2) is located in the secondary loop to aid in the filling and removing processes.

Table 3.1: Thermocouple Locations of the Scrooge 3.0 setup [36]. The T3 thermocouple is used for the Serpentine setup and is not relevant for this study. The T6-T8 thermocouples are located in the copper back panel of the window, with T6 giving feedback to the local power supply.

Thermocouple	Location
T1	Outlet Heat Exchanger
T2	Inlet Heat Exchanger
T4	Inlet Window
T5	Center Heated Tube
T6	Window
T7	Window
T8	Window

3. **Absolute Temperature Measurement**: The temperatures are measured at eight different locations throughout the setup via 0.5mm alumel-chromel thermocouples (type K, class 2, Labfacility) with a time constant of 0.9s on average. Each thermocouple is connected to National Instruments NI 9213 16-channel Thermocouple Input Module. The locations of the different thermocouples are given in table 3.1 and can be seen in figure 3.1 denoted by T1-T8. T3 is absent in the figure as it is used for another study.

Heated Tube

The red rod on the bottom tube in figure 3.1 is able to increase the temperature of the freon flowing through it. The tube is encased in a copper wire which can be put under large currents to generate ohmic heating. These currents are generated with a Delta SM15-200 (15V, 200A) power supply to generate a maximum power of 1 kW. 500-850 W is generally used as range to combat possible damage to the power supply system. This translates to a heat flux range of 19.9-33.9 kW/m^2 on the full tube.

Heat Exchanger

A simple heat exchanger is used to decrease the temperature of the freon inside the setup. This heat exchanger is connected to another separate heat exchanger. This second heat exchanger is connected to the cooling system of the RID building to export the heat generated in the setup.

Secondary Loop

Right above the bottom right corner are the connections to the secondary loop located as seen in figure 3.1. The secondary loop is used to add seeding to the main loop, to regulate the pressure and to fill and to remove the freon from the setup. A relieve valve is added as well in case the pressure exceeds the limits of the setup. Valves B-G are used to fill or empty the facility with freon from the tanks. Valves H-O are used to add seeding to the loop.

Traverser System

A traverser system is used to move the laser system in positon as shown in figure 3.4. This is done by using three independent motors to move in all three dimensions. The location of the measurement volume in the window depends on the location of the traverser. As the refractive indices of the different materials create refractions, a formula is used between the movement of the traverser and the movement of the measurement volume. This formula is a linear equation with a scale factor and an offset, which is derived in appendix A. As the offset is constant for all traverser locations, the laser intersection volume is only dependent on the scale factor of -0.15.

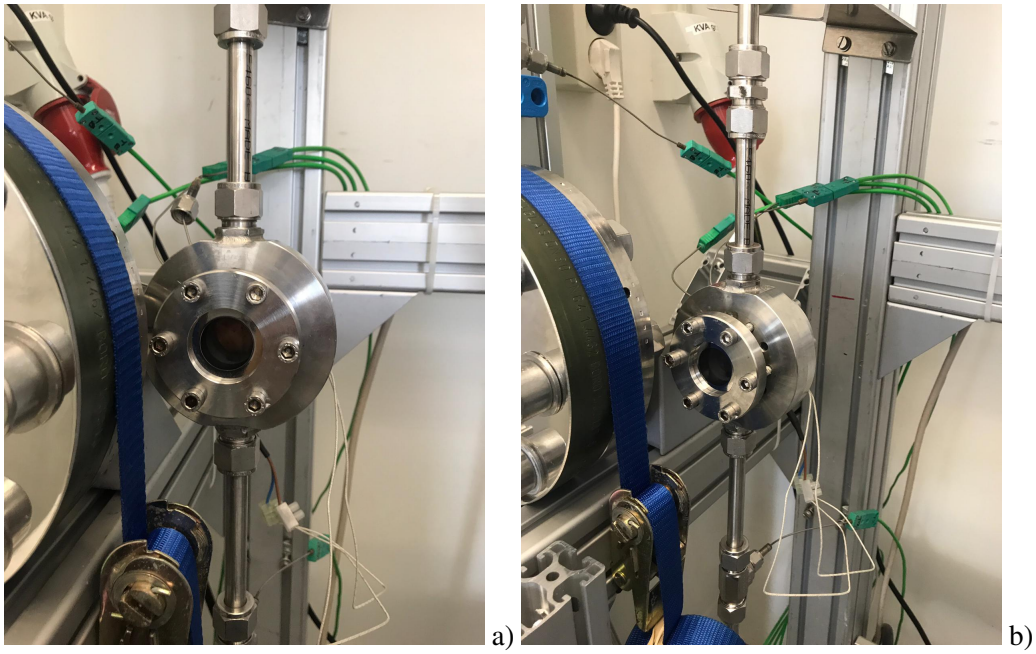

a) b)

Figure 3.3: Pictures of the window in the Scrooge 6.0 setup. A cylinder is held by a copper backside with heating elements incorporated and a front glass plane to give optical access to the freon. The green wires are the thermocouples wires which are connected to the thermocouples in the copper backside. To the left of the window is the Serpentine located, which is part of another study. ©*Y. Zheng*

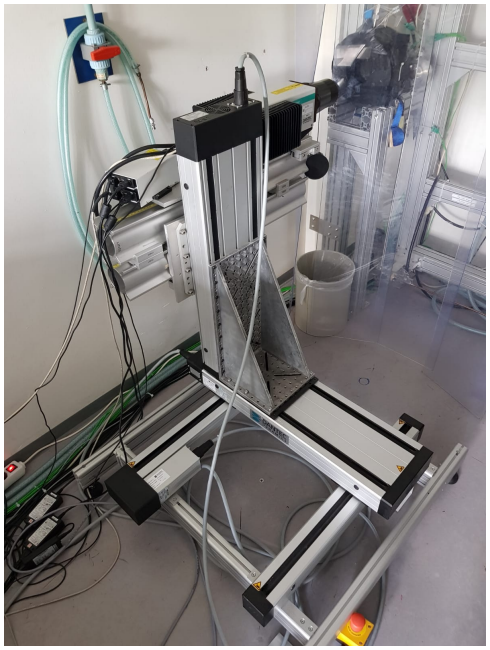

Figure 3.4: Picture of the traverser system which moves the lasers. The LDA lasers are mounted on the backside of the vertical traverser pointing the lasers to the measurement volume in the upper right corner.

Figure 3.5: Picture of the PC's which are used to control the setup (middle and right screen) and run the BSA Flow software (left screen) [38]. The processor is located beneath the right screen.

3.1.4 External Components and Systems

Several extra external components and systems are used to control the setup. These systems ensure safety for the operators and are separate from the loop.

Pressure Control

The pressure is controlled via two Parker Series 5000 Piston Accumulators which are separately connected to a third network filled with pressurized air. One piston is connected to the main loop and has an electronic circuit to indicate the position of the piston inside via a number (0-15). The second piston is connected to the secondary loop for the recovery system. The third air network is connected to a pressurized air tank and to an exit valve to release the pressure.

Power Supply Safety System

All signals are connected to either a Thermocouple Module (thermocouples) or Data Acquisition Board (pressure). Data is acquired by means of a labview program [37] which has access to the sensors and has several safety parameters built-in to prevent the setup from damaging itself. If the temperature or the pressure reaches a certain preset level, the power supplies of the setup will be switched off and no further heating (and therefore increase of pressure) can happen. The power supplies can only be turned on again after the reset button is manually pressed.

Recording System

The sensor data and safety data is recorded on a PC with one National Instruments NI 6036 Data Acquisition Board and one USB National Instruments NI 9213 16-channel Thermocouple Input Module. The measured signals can be recorded and together with the processed data displayed on the screen of the PC as shown in figure 3.7.

Vacuum Pump

Before pure freon can fill the setup, it has to be evacuated. This is done with a Micronite Lite MK-50-DS vacuum pump.

Freon Recovery System

It is for environmental reasons not recommended to release freon in the air. Therefore, the freon must be recovered when the setup needs to be opened. However, a system to recover all the freon does not exist yet. After decreasing the pressure and temperature, the freon separates in a liquid and

vapour state. The liquid freon is easily removed using the pistons to push the liquid into the high pressure containers. This has to be done several times to decrease the pressure and to empty the setup. However, the vapour freon is much harder if not impossible [36], so a bit of freon escapes when the setup is opened.

Cooling Stabilization

The freon is cooled down via the heat exchanger located in the top tube. The cooling water that flows through the heat exchanger is separately cooled down by a second exchanger to stabilize the temperature of the cooling water. The second exchanger is connected to the RID building Cooling System.

3.1.5 LDA Placement

The LDA is placed facing the measurement volume (left side of the loop in figure 3.1) and is positioned orthogonal with respect to the glass window. However, the lasers have a wavelength in the visible light range, which means that the particles of the fluid are to small to be detected and therefore no reflections will be seen. Seeding will be added to the fluid flow to accommodate this problem, see section 3.2. The reflection that is given by the seeding particle will then be captured by the receiving optics and guided to a photo multiplier detector via optical fibers and there translated to current pulses which will be interpreted by a computer. Each measurement only takes place in one spatial location meaning the LDA must be translated in all three dimensions to measure all points in the total measurement volume. The LDA is placed on a single traverser, which is the reason for using the crossbeam mode. The whole installation will be moved by the computer controlled traverser in a predefined path throughout the total measurement volume.

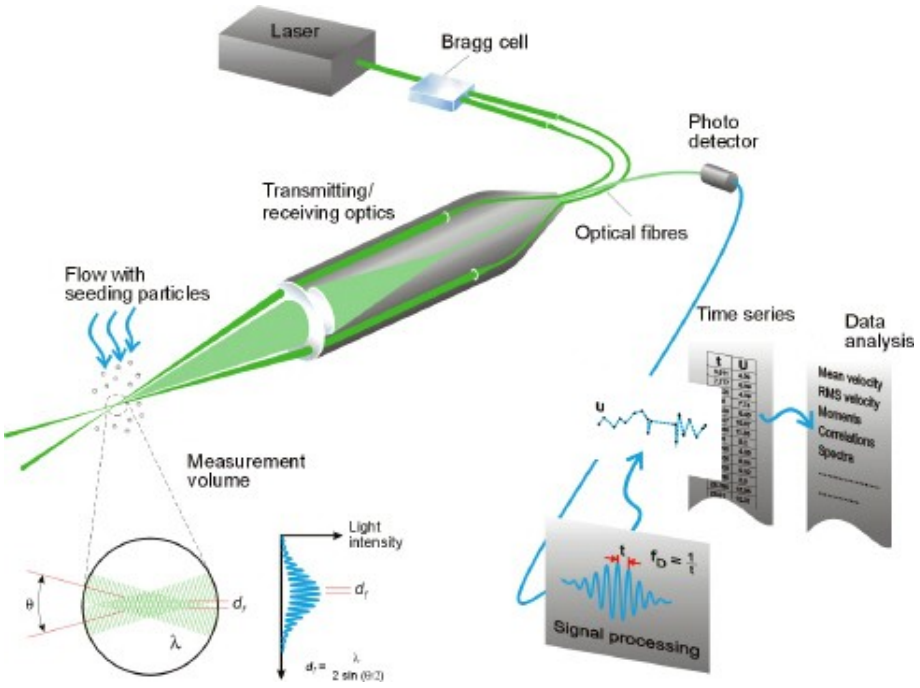

Figure 3.6: The workings of a Laser Doppler Anemometry system. The laser is splitted by a Bragg cell in two coherent laser beam which are sent towards an intersection at the exact spot of measurement via an optic system. Particles that flow through this intersection will create a reflection which will be received by the photo detector and analyzed [39].

Figure 3.7: Picture of the two cooling installation used in both Scrooge setups. The left installation is the secondary loop, which is connected to the internal cooling system of the building. The right installation is the disconnected cooling installation, which regulates itself.

3.1.6 Scrooge 6.0

After modifications to the setup, a parallel setup was added to accommodate the Serpentine used in another study. This resulted in a change in the thermocouples with the T3 thermocouple especially located at the Serpentine unit. The T4 thermocouple was set closer to the window inlet for more accurate conditions. A separate cooling installation was added as well to create more independant and stable conditions. The Serpentine unit is a separate measurement volume used in a study on heat transfer in a special geometry.

3.2 Seeding

The molecules of freon are too small to create reflections by visible light. Therefore tracer particles or seeding is added to the freon, which are small particles that flow with the freon, but can scatter the light and therefore allow measurements with optical techniques. To measure the velocity of the fluid as accurate as possible, the difference in velocity between the fluid and the particles should be as low as possible. Stokes' drag law in equation shows the relationship between the densities of the particles, the density of the fluid and the difference in velocity $\vec{U}_{slip}$ [40]:

$$\vec{U}_{slip} = \vec{u}_p - \vec{u}_f = d_p^2 \frac{\rho_p - \rho_f}{18\mu} \vec{a} \tag{3.3}$$

Here, d_p is the diameter of the particle, ρ_p the density of the particle, $\vec{a} = \frac{\vec{F}}{m}$ the acceleration of the particle and μ and ρ_f the dynamic viscosity and density of the fluid. To reduce U_{slip}, either the particle diameter must be reduced, or the densities must closely match [6]. A constraint on the size of the particles is the ability to reflect the lasers, the particles need to be large enough to scatter the lasers.

Stokes' drag law has the restriction of being valid for very low Reynolds numbers. At higher

Reynolds numbers, the formula becomes more complex and results in the BBO-equation by Joseph Valentin Boussinesq, Alfred Barnard Basset and Carl Wilhelm Oseen [41, 42, 43] as shown in formula 3.4:

$$\frac{\pi}{6}\rho_p d_p^3 \frac{d\vec{u}_p}{dt} = 3\pi\mu d_p(\vec{u}_f - \vec{u}_p) - \frac{\pi}{6}d_p^3\vec{\nabla}P + \frac{\pi}{12}d_p^3\rho_f\frac{d}{dt}(\vec{u}_f - \vec{u}_p) + \frac{3}{2}d_p^2\sqrt{\pi\rho_f\mu}\int_{t_0}^{t}\frac{1}{\sqrt{t-\tau}}\frac{d}{d\tau}(\vec{u}_f - \vec{u}_p)d\tau + \frac{\pi}{6}d_p^3\vec{g}(\rho_f - \rho_p) \quad (3.4)$$

Here, P is the pressure and $\vec{g}$ the gravitational vector with $\vec{g} = (0,0,9.81)^T$ m/s^2. The first term, before the =-sign, is the acceleration term. After the =-sign, the Stokes' drag term, the pressure term, the added mass term, the Basset history term and the bouyancy term are present. However, this formula is too complex to use for this study, therefore the simpler Stokes' drag law will still be used. Their effect was studied by Mei (1996) [44] with a frequency response analysis of the particle to a sinusoidal oscillation of the free stream. They found that a good response for seeding particles was found where the density ratio between seeding patricle and fluid $\rho_p/\rho f$ between 0.56 and 1.62 [44].

Particles with different properties can reflect differently, which causes different scattering patterns. Possible properties that can be different are: size of the particle, the material, the density, etc. These options give countless property variations that can be made to see their effects on the flow inside the setup. This study will focus on four different particles with the same properties except for their density. These densities will be further explained in chapter 5.

3.2.1 Insertion of Seeding

The seeding can be inserted in the loop both via a secondary loop and via an extra seeding tank. Between valves J and K in figure 3.1 there is a hatch to insert the seeding. Both valves need to be closed and the hatch can be opened. After closing the hatch valve H can be closed to divert the freon loop via the hatch and opening valves J, K, N and O will create the diverted loop to let the seeding enter the flow. After a short time valve H can be opened and valves J, K, N and O be closed to let the flow continue through the main loop. The seeding can also be inserted via the extra tank connected between valves N and O. Closing these valves and disconnecting, filling and reconnecting the filled tank allows for inserting. After this the tank can be vacuumed of air via the piston system and valve G. The vacuumed tank can then be used as part of the secondary loop in the same way as before. The advantage of removing and replacing the tank is the minimum amount of air that is inserted inside the main loop by vacuuming the tank before implementing. The disadvantage is that the removal and reconnecting allows for the facility to be possibly damaged during replacements.

3.3 Processing the Data

While running the LDA, data is acquired through the receiving optics and the processor. This data is acquired randomly as the reflecting seeding particles will not always be present or reflect towards the receiving optics. The received samples therefore need to be processed before they can be plotted. The data processing is done in three steps. The data is filtered of reflections. This is done by an inverse band gap filter. Secondly, the wanted variables are calculated. For example, the mean and the RMS values. Lastly, the data is resampled to obtain the confidence intervals of the wanted variables. This is done by the Jackknife method. With these confidence intervals, the values can be visualized with a confidence interval. The mathematics behind these steps will be done in the appendices: the filtering and calculating steps will be done in appendix B.1 while the

resampling step will be done in appendix B.2.

The jackknife method results in a confidence interval of the estimator $\hat{\theta}$ of 95% within the interval $\hat{\theta} \pm 1.96\sqrt{\text{var}(\hat{\theta})_{jack}}$ [45]. Here, the estimators will be the mean velocities $\overline{u}$ and $\overline{v}$.

4. Simulations

Stream of Water ©J. Wetts [46]

Before starting the measurements, it is helpful to simulate how the fluid will behave in the geometry of the window. This way a rough idea of the complex flow through the measurement volume can be visualized.

4.1 Simulation Setup

The Computational Fluid Dynamics (CFD) program FLUENT from ANSYS [11] is used to model the experimental setup. The simulations will be used as a more accurate reference to the measurements than the free jet approach from section 2.3. The geometry is shown in figure 4.1. The lengths of the geometry have been measured and the details are tabled in table 4.1.

Table 4.1: The measured radii r, lengths L and tilts θ in the geometry. The length of the inlet and outlet tubes is defined as the minimum length between the outside to the window cylinder.

Dimension	Length
r_{window}	10 mm
L_{window}	25 mm
r_{inlet}	5 mm
L_{inlet}	100 mm
r_{outlet}	5 mm
L_{outlet}	100 mm
Tilt θ_r	$-0.5° \pm 0.05°$
Tilt θ_y	$+0.9° \pm 0.05°$

Several deviations were found in the setup in the tilts of the inlet tube. The inlet tube was tilted compared to the normal vector of the cylinder. A slight tilt in the x-direction and the y-direction was observed. The tilt was measured to be -0.5° in the r-direction and +0.9° in the y-direction.

The geometry was divided in a mesh of 1.6×10^6 elements to simulate the flow. As the properties of freon vary with temperature, several simulations were done to measure the difference per inlet temperature. Gravity at $g = 9.81$ m/s was incorporated in the simulations in the reverse flow direction ($-X$-direction). The solutions all converged after about 100 iterations.

4.2 Results

The simulations were compared with the experimental data at several relevant locations. The centerline in the r-direction was probed in section 4.2.1. The center points of the interfaces between the inlet/outlet tube and the window were probed as well. This is done in section 4.2.2.

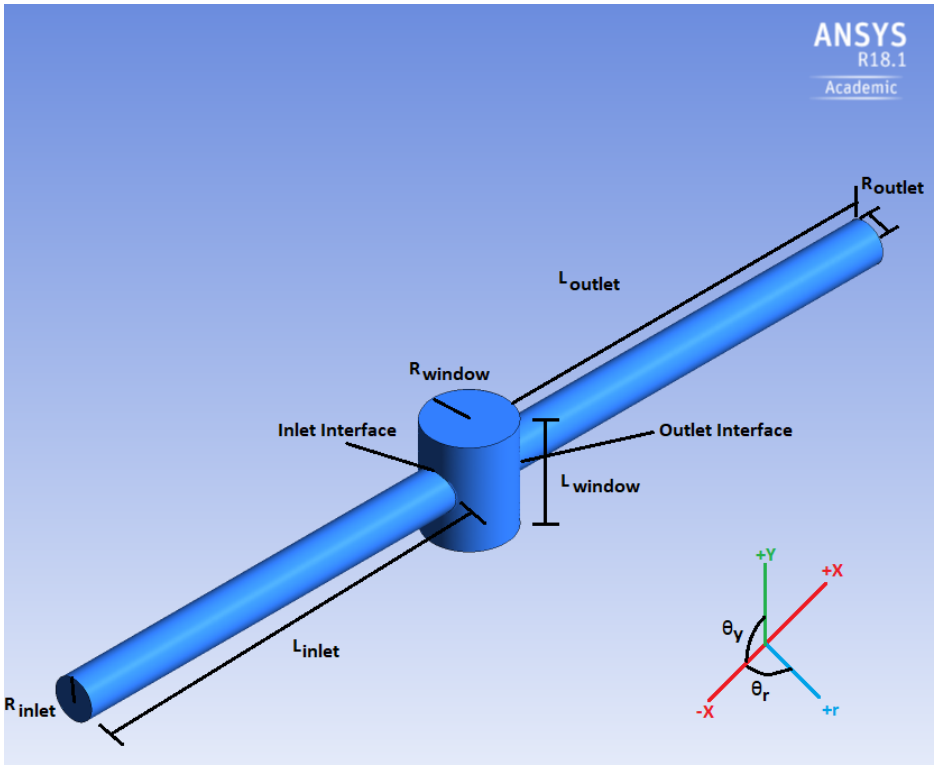

Figure 4.1: Geometry of the setup that is used in the simulations. The inlet tube is slightly tilted in accordance with the real experimental setup. Here, the angles θ_r and θ_y are defined as the angle from the respective positive r-axis and positive y-axis towards the positive x-axis. The tilt is -0.5° in the r-direction and +0.9° in the y-direction. The dimensions are tabled in table 4.1. The center of the axes is located in the middle of the measurement volume. Therefore the measurement volume has the following dimensions: $-12.5 \leq y \leq 12.5$, $-10 \leq r \leq 10$ mm and $-10 \leq x \leq 10$ mm. Here, tube stands for both inlet and outlet.

4.2.1 Centerline

In figure 4.2 the results for the so-called centerline are shown. The centerline is located from (0,0,-10 mm) to (0,0,10 mm) in the (x,y,r). A nearly symmetrical solution is found for every temperature. This indicates that the deviation of the inlet tube has a small effect on the converged solution. However, the solution is significant different from the free jet approach solution from section 2.3. This is due to the constraints at the free jet approach, which allowed for the solution if the outer area was 10^5 times larger than the nozzle area. The simulated velocity profile allows the no-slip wall constraints of the measurement volume. As explained in section 2.3.1, the density of freon decreases as the temperature rises, therefore the average velocity increases, which explains the different profiles for the different temperatures as shown in figure 4.2.

The absolute differences between the sides can be seen in figure 4.3. As can be seen, all temperatures have the largest deviations from symmetry around $r = \pm 0.2$ cm. This is most likely around the edges of the jet stream. The tilted jet stream would give a difference around the edges since the edge is at a different position. This will give rise to the differences.

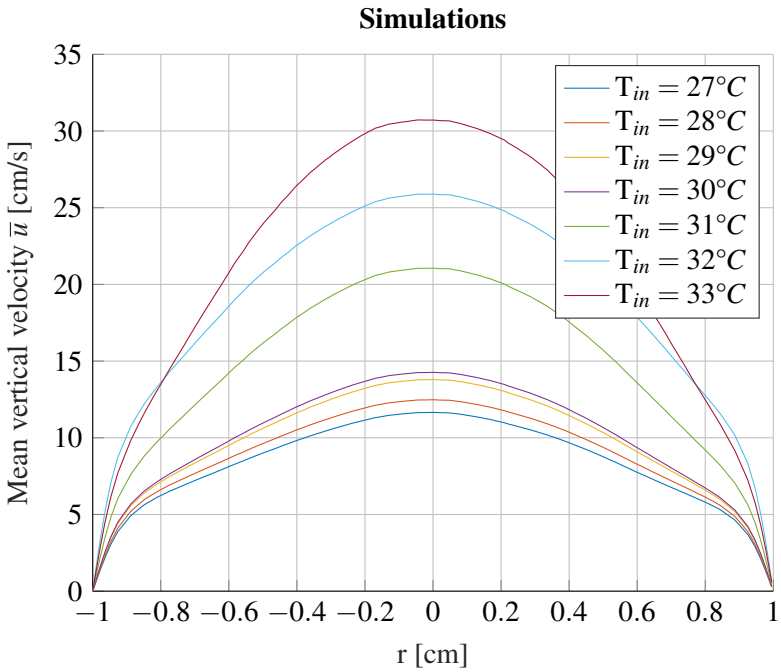

Figure 4.2: Simulations results of the centerline in the r-direction, the vertical velocity is taken in the flow direction.

4.2.2 Inlet/Outlet Interfaces

The inlet and outlet velocities are tabled in table 4.2. These points represent the centerline velocity of the flow at the inlet interface and the outlet interface as shown in figure 4.1. The inlet velocity will be used as a reference velocity for the unitless velocity u_{XX}/u_s, with XX for inlet/outlet/vert,max. These unitless velocity ratios are called the Velocity Ratios (VRs) and are calculated for the inlet velocity u_{in}, outlet velocity u_{out} and the maximum vertical velocity on the centerline $u_{vert,max}$. The VRs can be seen in the columns next to their respective velocity.

The VRs are used to indicate a constant of proportionality between the simulated variable

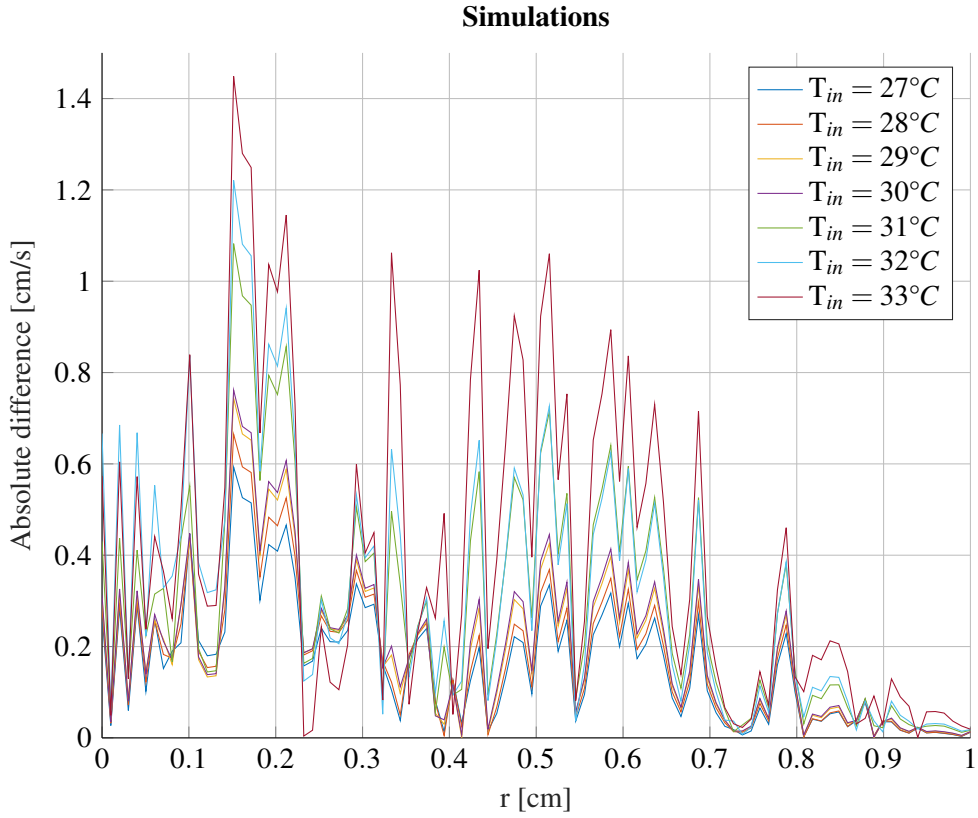

Figure 4.3: Absolute difference in velocity between the left and the right side of the window. A maximum is calculated most likely near the edge of the jet stream. This is due to the deviation in the inlet tube, which causes a tilted jet and therefore asymmetric jet stream edge positions.

Table 4.2: Seven simulations done at different inlet temperatures. The vertical inlet velocity u_{in} and vertical outlet velocity u_{out} at the center of the interface between the window cylinder and the respective tube is given for every simulated inlet temperature. The inlet velocity u_s, calculated with equation 2.4 from the free jet approximation, is given for every inlet temperature as well. The maximum velocity on the centerline, centerline $u_{vert,max}$ and the Velocity Ratios (VRs) for each velocity are added for completion.

T_{in}	u_s	u_{in}	u_{in} VR	u_{out}	u_{out} VR	$u_{vert,max}$	$u_{vert,max}$ VR
27°C	33.7 cm/s	44.84 cm/s	1.33	37.39 cm/s	1.11	11.7 cm/s	0.345
28°C	35.7 cm/s	47.70 cm/s	1.34	39.68 cm/s	1.11	12.5 cm/s	0.350
29°C	39.2 cm/s	51.88 cm/s	1.32	42.98 cm/s	1.10	13.8 cm/s	0.316
30°C	47.7 cm/s	53.28 cm/s	1.12	44.16 cm/s	0.926	14.3 cm/s	0.299
31°C	58.8 cm/s	72.88 cm/s	1.24	60.31 cm/s	1.03	21.1 cm/s	0.358
32°C	66.7 cm/s	85.57 cm/s	1.28	75.34 cm/s	1.13	25.9 cm/s	0.388
33°C	72.3 cm/s	97.70 cm/s	1.35	81.21 cm/s	1.12	30.7 cm/s	0.425

(such as u_{in}) and a given condition. This proportionality would allow to interpolate the velocities if a reference is needed for an intermediate temperature, for example, 29.6°C. This way, it would not be necessary to simulate every case separately if the inlet temperature is slightly different.

As can be seen in table 4.2, the VRs for u_{in} are constant with an average of 1.28 ± 0.16, which is 12.5%. The average of the VRs of u_{out} equals 1.07 ± 0.14, which is 13%. Finally, the VRs of $u_{vert,max}$ have a more spread out result. An average of 0.360 ± 0.065 equals 18% uncertainty. In the 30°C case, the temperature is close to the pseudocritical temperature for 53 bar. This results in heavily changing material properties and therefore the simulations might be slightly off. Therefore it might be feasible to discard this simulation as unrealistic. If the u_{in} VR of the 30°C simulation is skipped, the average of the VRs results in 1.31 ± 0.07, which is 5.3% and a more acceptable uncertainty. For u_{out}, removing the 30°C case results in an average of 1.10 ± 0.07, which is 6.3% and therefore has a significant reduction in the uncertainty compared with the former situation. However, removing the 30°C case for the $u_{vert,max}$ VR, results in 0.370 ± 0.055, which is still 15%. This means that the removal of the 30°C case does not improve the uncertainties for all statistics, which means that the case cannot be discarded. Therefore, if an intermediate reference is needed, the simulation which is closest to the inlet temperature will be used.

5. Seeding Measurement Results

Flow ©Flow Control Network [47]

A number of measurements were done to indicate the compatibility between the conditions of the freon and several different seeding types. This study will focus on the aspect of density of the particles. Four different densities will be used to see their effects: 1 g/ml, 0.79 g/ml, 0.55 g/ml and 0.36 g/ml. These four densities encapsulate the density range of the freon around the pseudocritical temperature at a pressure of 53 bar as shown in figures 2.2.g and 2.4. Two separate measurement types are done: isothermal measurements to show the feasibility of the different seeding types and locally heated measurements to show the feasibility of LDA in volumes with changing densities. The isothermal measurements are shown in section 5.2-5.4. The locally heated measurements are shown in section 5.5.

5.1 Measurement Locations

The measurements were performed in the measurement volume, also known as the window. Here, the cylindrical measurement volume of the loop is meant, not the laser intersection volume of the LDA. Due to time constraints, it is not possible to analyze the whole volume in detail. Therefore several locations of interest have been chosen for analyzing. These points are shown in figure 5.1. The inlet and outlet points are located near the the interface between the window and the tube leading inwards or outwards. These points are located in accordance with their simulated counterparts in section 4.2.2 and table 4.2. The green points represent the centerline and the dark blue points the depth-line, to analyze the depth differences. The centerline is located at the center height ($x = 0$ mm), center depth ($y = 0$ mm) and stretches from $r = -8$ mm to $r = 8$ mm. The radial boundary was not measured due to the physical constraints of the horizontal pair of lasers. The depth-line is at center height ($x = 0$ mm), center width ($r = 0$ mm) and stretches from $y = -10$ mm to $y = 10$ mm. The inlet and outlet points are placed at $x = -8$ mm and $x = 8$ mm, respectively, and both at $r = y = 0$ mm.

The measurement points are sequentially measured by the LDA with the traverser translating the LDA in the right position.The traverser has had slight problems with the vertical motor in increasing the laser height. Therefore, the measurements were done in decreasing height order (negative x-direction), starting with the outlet interface and ending with the inlet interface measurement. The depth-line and the radius-line are measured in between the inlet and outlet at the center height ($x = 0$ mm).

5.2 Results Centerline

The centerline provides valuable information about the flow of the freon inside the window as the line is perpendicular to the LDA lasers and perpendicular to the flow direction. Therefore both measurable velocities can give valuable information about the complex flow. The depth-line

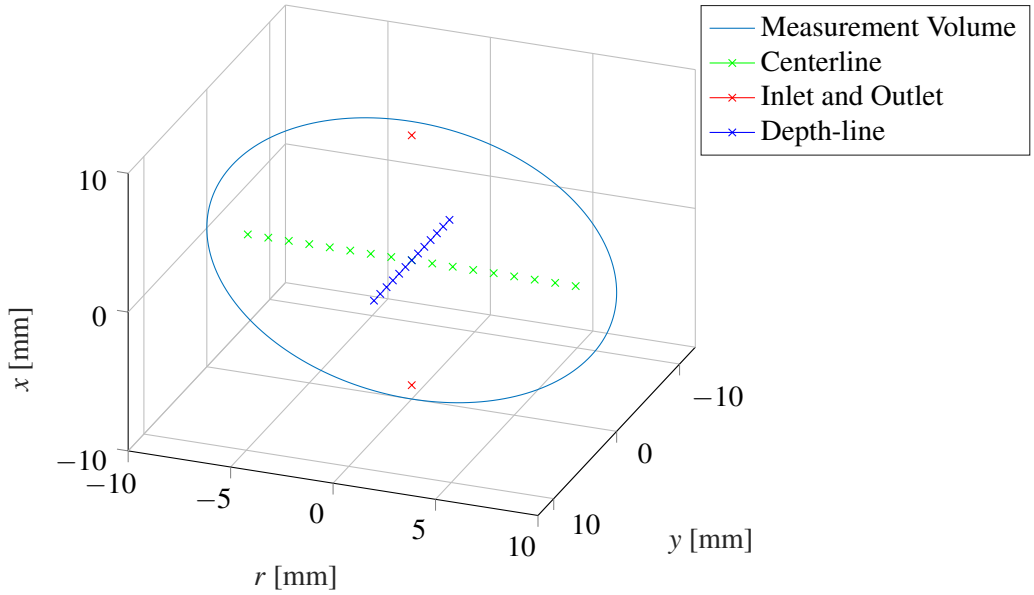

Figure 5.1: The used measurement points. The LDA enters the measurement volume from the window in the front at $y = 12.5$ mm. The blue circle represents the measurement volume boundary in the radial direction. The dark blue centerline has measurements values from $r = -8$ mm to $r = 8$ mm. This is due to the refraction at the edges, which obstruct the reflections from reaching the LDA or creating reflections at all. The inlet and outlet points are placed at $x = -8$ mm and $x = 8$ mm, respectively, and both at $r = y = 0$ mm.

also gives valuable information, but is not perpendicular to the LDA direction, so no data can be obtained of the related velocity component $\overline{w}$. The following figures (figure 5.2-5.7) have the vertical velocities $\overline{u}$ plotted against the centerline. For completion, the mean velocities are denoted as $(\overline{u}, \overline{v}, \overline{w})$ for (x, r, y).

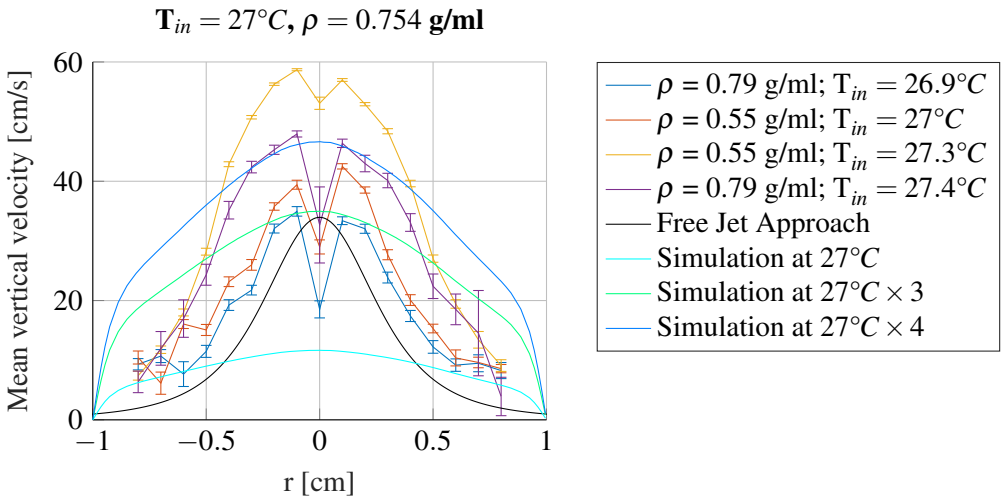

Figure 5.2: Several measurements done around an inlet temperature $T_{in} = 27°C$. The freon density at these conditions is 0.754 g/ml [34]. The inlet velocity of the simulation is $u_s = 33.7$ cm/s, calculated with equation 2.4 with a massflow $\dot{m} = 20 \pm 0.5$ g/s as measured with the Coriolis meter. The simulated velocities times three and four are added as well.

The freon density at a temperature of 27°C and 53 bar is 0.754 g/ml [34]. Therefore the seeding with density 0.79 g/ml would be expected to have the greatest accordance with the simulations. However, the simulated velocities are much lower compared with all experimental data as seen in figure 5.2. A bell-shaped curve is seen with the confidence intervals for the values. A similar curve is found for every measurement, even with different seeding types, but the amplitudes of the velocity differ greatly. The shape of the inaccurate free jet approach is more alike than the shape of the simulations. These shape comparisons are made without experimental data on the window edges, as it was not possible to acquire data in those regions. Between the measurements of the same seeding type, a large difference can be found. The blue and magenta measurement in figure 5.2 are done with the same type of seeding, 0.79 g/ml, but on a different day. The same is seen for the yellow and red measurements with type 0.55 g/ml. These were measured on different days as well. However, as the inlet temperature is different, a different velocity amplitude is expected.

The simulated data multiplied by a factor is added as well. These modified simulation velocities show that the experimental data is far off of the simulation data. The maximum velocities occur at about 3-4 times the maximum simulated velocity, but away from the center the velocity profiles do not match at all. This indicates that the simulations seem to contain errors, the experimental data is flawed or both apply.

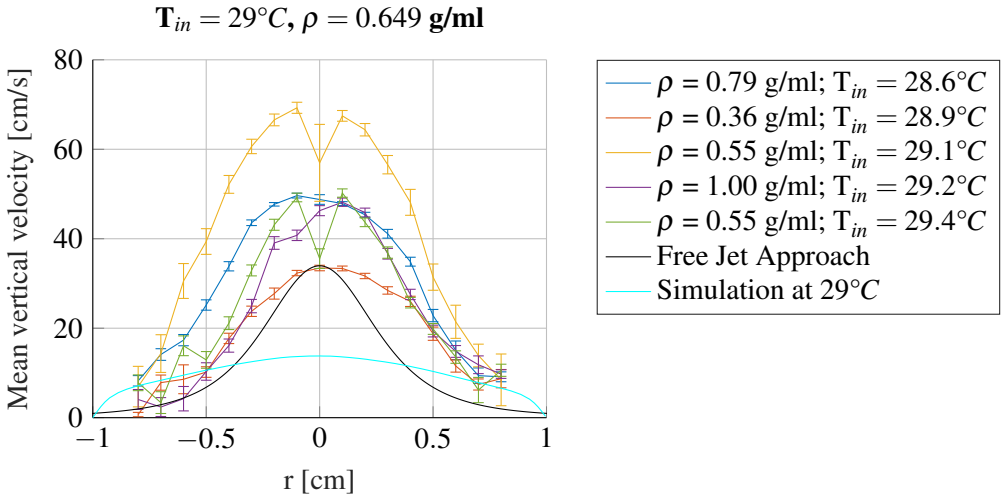

Figure 5.3: Several measurements done around an inlet temperature $T_{in} = 29°C$. The freon density at these conditions is 0.649 g/ml [34]. The inlet velocity of the simulation is $u_s = 39.2$ cm/s, calculated with equation 2.4 with a massflow $\dot{m} = 20 \pm 0.5$ g/s as measured with the Coriolis meter.

The same can be seen for the measurements at 29°C in figure 5.3 as the simulation has a much lower amplitude than the experimental data. The results for the measurements at higher supercritical temperatures show even more discrepancies between the simulated velocities and the experimental data. This is seen in the following figure: figure 5.4 for the data at inlet temperature $T_{in} = 30°C$, figure 5.5 for $T_{in} = 31°C$, figure 5.6 for $T_{in} = 32°C$ and finally figure 5.7 for $T_{in} = 33°C$.

As no local heating is applied in these measurements, there should be no difference in the discrepancies between the simulated velocities and the measured velocities. Because the temperature does not change within the measurement volume, there is a single density present.

It is observed that the velocity profile measurements with inlet temperatures above the pseudocritical

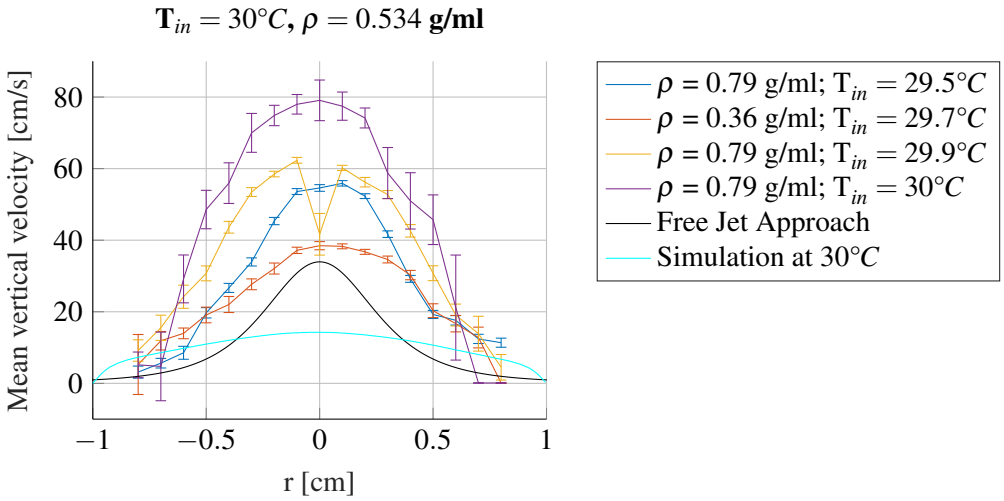

Figure 5.4: Several measurements done around an inlet temperature $T_{in} = 30°C$. The freon density at these conditions is 0.534 g/ml [34]. The inlet velocity of the simulation is $u_s = 47.7$ cm/s, calculated with equation 2.4 with a massflow $\dot{m} = 20 \pm 0.5$ g/s as measured with the Coriolis meter.

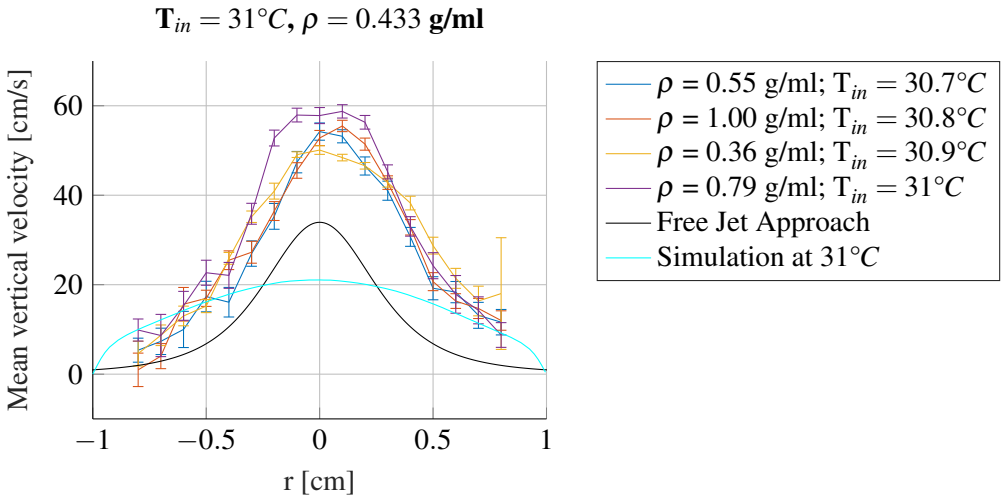

Figure 5.5: Several measurements done around an inlet temperature $T_{in} = 31°C$. The freon density at these conditions is 0.433 g/ml [34]. The inlet velocity of the simulation is $u_s = 58.8$ cm/s, calculated with equation 2.4 with a massflow $\dot{m} = 20 \pm 0.5$ g/s as measured with the Coriolis meter.

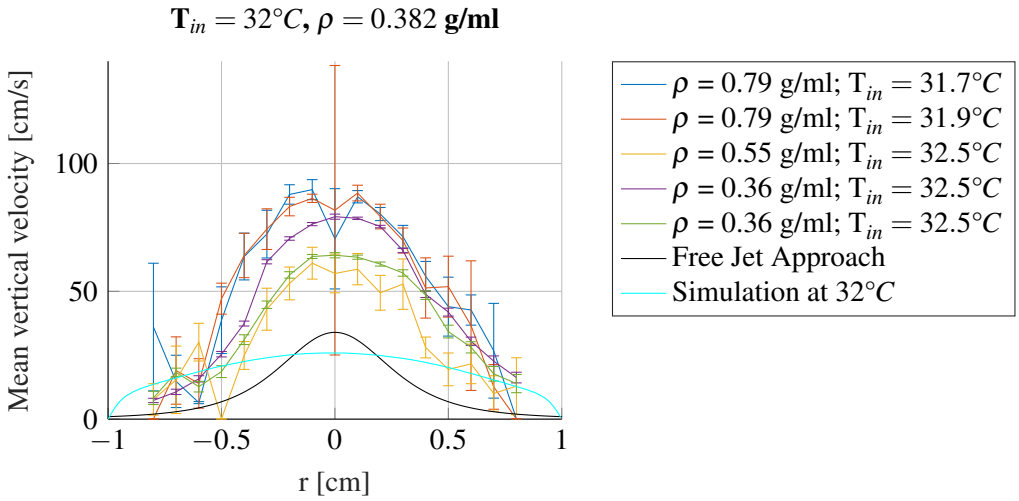

Figure 5.6: Several measurements done around an inlet temperature $T_{in} = 32°C$. The freon density at these conditions is 0.382 g/ml [34]. The inlet velocity of the simulation is $u_s = 66.7$ cm/s, calculated with equation 2.4 with a massflow $\dot{m} = 20 \pm 0.5$ g/s as measured with the Coriolis meter.

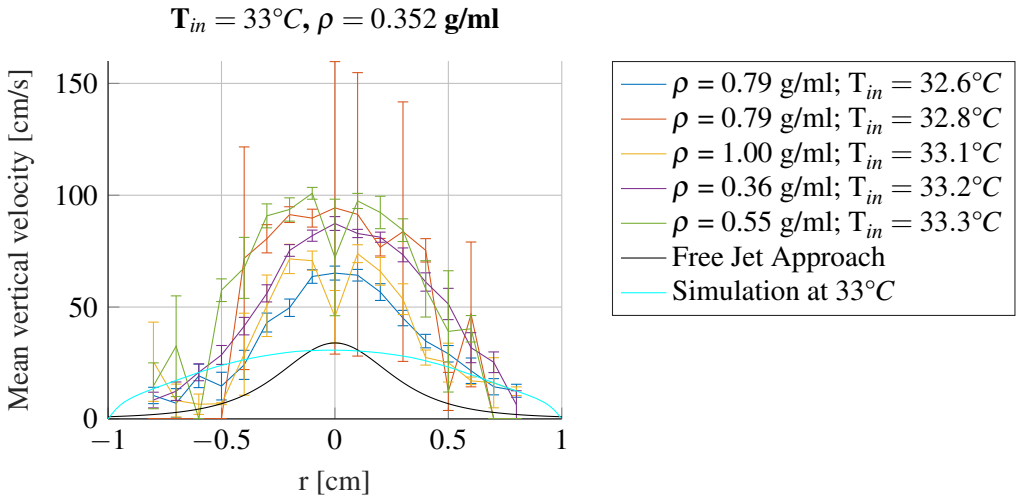

Figure 5.7: Several measurements done around an inlet temperature $T_{in} = 33°C$. The freon density at these conditions is 0.352 g/ml [34]. The inlet velocity of the simulation is $u_s = 72.3$ cm/s, calculated with equation 2.4 with a massflow $\dot{m} = 20 \pm 0.5$ g/s as measured with the Coriolis meter.

point T_{pc} match significantly better with each other than below the pseudocritical point. Especially in the $T_{in} = 31°C$ case all four measurements have almost the same velocity profile. As said before, this should not matter as only a single density of freon is present. Therefore it is remarkable that accordance is shown among the experimental data. As the slip velocity U_{slip}, as explained in section 3.2, is dependent on the difference in density, the different seeding particles should give different slip velocities. Therefore other points of interest and the horizontal velocity $\overline{v}$ need to be explored.

5.2.1 Horizontal velocity

Coincidentally with the vertical velocity, the horizontal velocity was measured at the same locations. The direction of the horizontal velocity is equal to the r-direction, which means a positive horizontal velocity is rightwards and a negative velocity leftwards. This is further shown in section 5.2.2 with vectorplots. As shown in figures 5.8 and 5.9, a similar velocity profile seem to exist at all different inlet temperatures. The similar velocity profile indicates the absence of significant flow altering events when changing the inlet temperature, which is in accordance with the simulations.

Several zero crossings happen at every temperature range, these may indicate a pure vertical flow, albeit that the depth velocity $\overline{w}$ in the y-direction cannot be known. The different seeding particles do not seem to give a significant different result, as the confidence intervals have overlap with each other at nearly every measurement point. This indicates a lower slip velocity in the horizontal direction, which might be due to a difference in horizontal force on the seeding particles.

5.2.2 Vectorplots

The vectorplots allow for a visualisation of the flow direction. The different measurements per temperature case are displayed above each other with their measurement number at the vertical axis. This way the vertical axis has no other purpose than visualising the different measurements. The lengths of the arrows are purely for comparison as the different velocities can be checked in their respective vertical velocity and horizontal velocity graphs. In many plots the M-shaped profile can be seen in the arrows. It is shown in all vectorplots in figures 5.10-5.12 that the flow is moving towards the x-axis. No circulations are found as there are no downwards measured flow velocities in any of the measurements. The general profile of the different plots is a bell curve, which is best visible in the cases at $29°C$ to $31°C$ in figures 5.10.b and 5.11.

In the lower density region ($\rho_{freon} < 0.4$ g/ml) at $32°C$ and $33°C$, the profile becomes less smooth. The higher density seeding particles create edge regions with local peaks in velocity. Especially the 0.79 g/ml measurements at $32°C$ (figure 5.12.a, blue and red lines) and the 0.79 g/ml and 1.00 g/ml measurements at $33°C$ (figure 5.12.b, blue, red and yellow measurements) create edge regions that are different than the bell curve profile of most measurements. These differences may be a result from a complex three dimensional flow, but may also be the result of a larger slip velocity due to the larger density differences.

5.3 Results Inlet/Outlet Interfaces

Another duo of interesting points to measure are the interface between the inlet and the window and the interface between the outlet and the window as shown in figure 4.1. Taking the centerpoints of these interfaces gives a measure to compare the simulations with the experimental results. The inlet and outlet interfaces allow for benchmarks as the flow is still a partially developed turbulent flow at the inlet interface and returns to a turbulent flow at the outlet interface.

As an inlet temperature of $27°C$ is well below the critical point of freon, a high degree of similarity

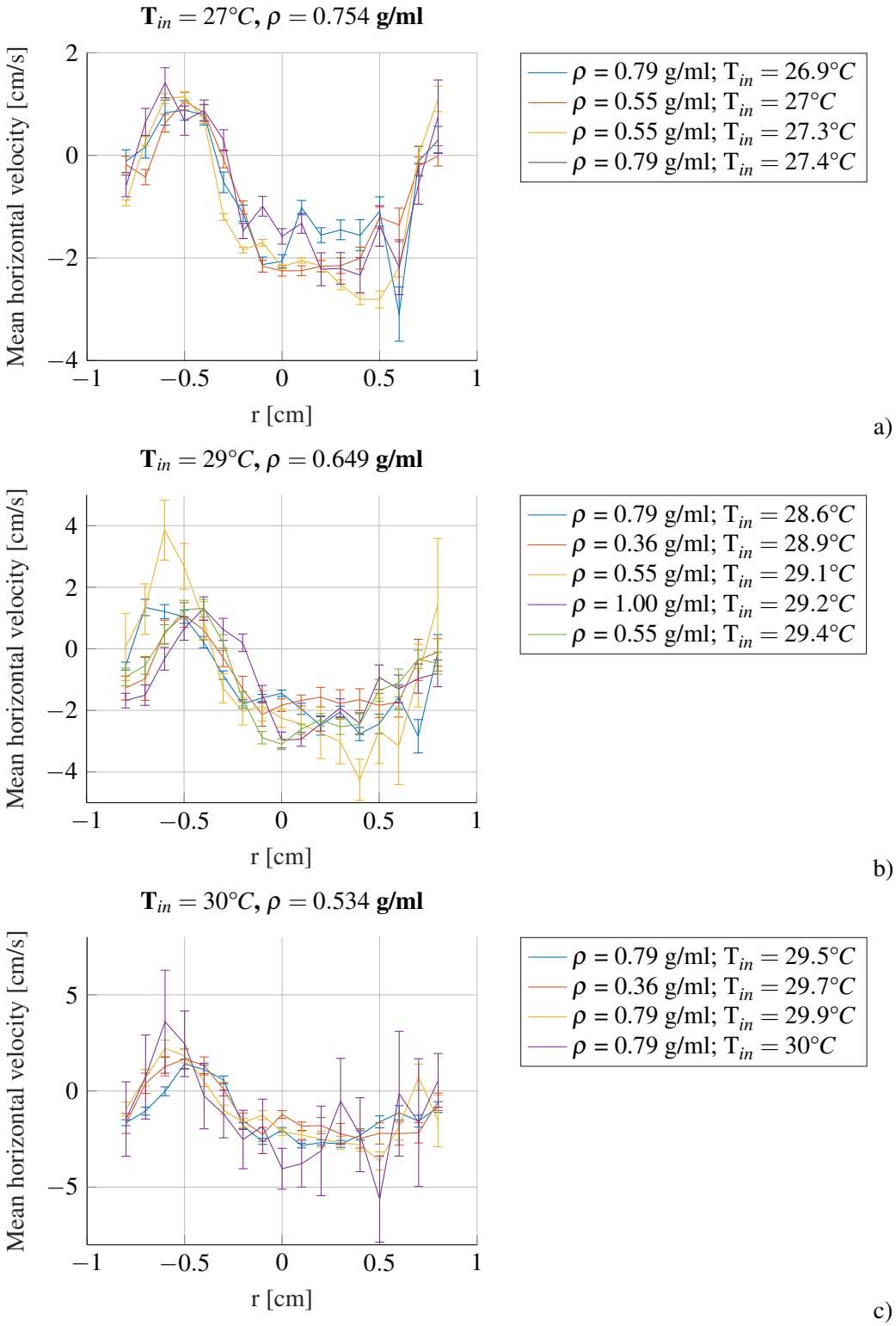

Figure 5.8: Horizontal velocity in the r-direction at the same locations as figures 5.2-5.4. The horizontal velocities are measured at the same coincedence intervals as the vertical velocities. A positive horizontal velocity signifies a flow in the positive r-direction (to the right).

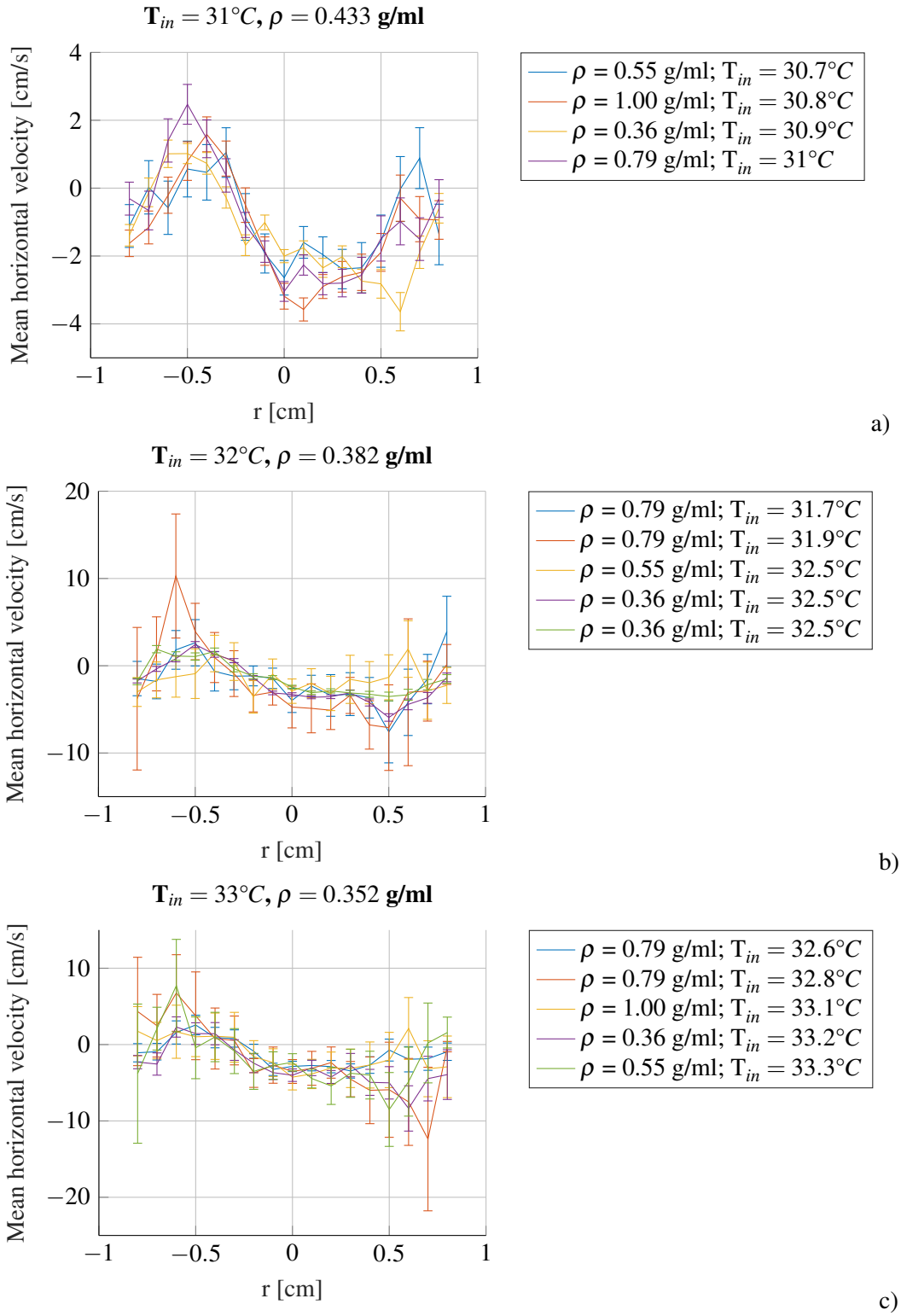

Figure 5.9: Horizontal velocity in the *r*-direction at the same locations as figures 5.5-5.7. The horizontal velocities are measured at the same coincedence intervals as the vertical velocities. A positive horizontal velocity signifies a flow in the positive *r*-direction (to the right).

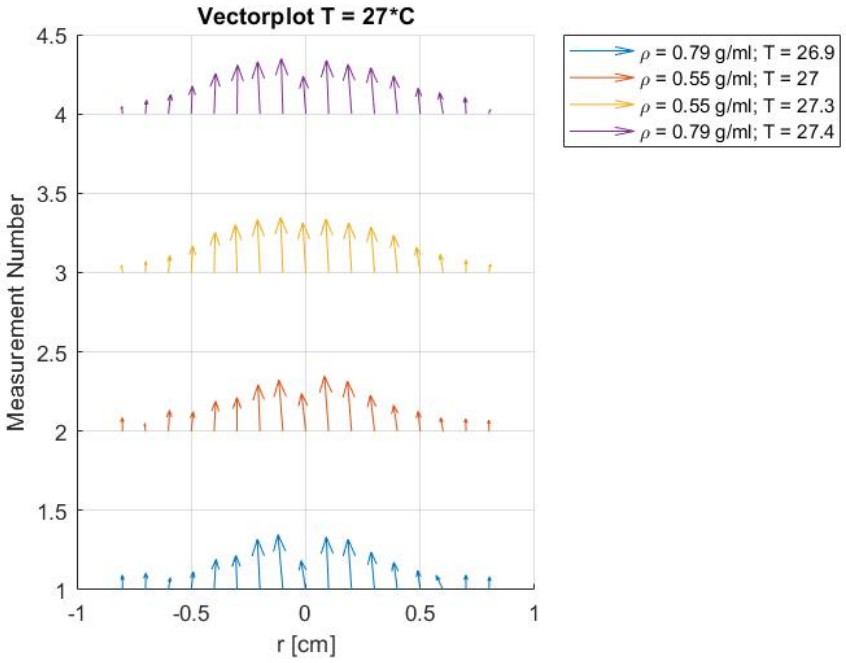

a)

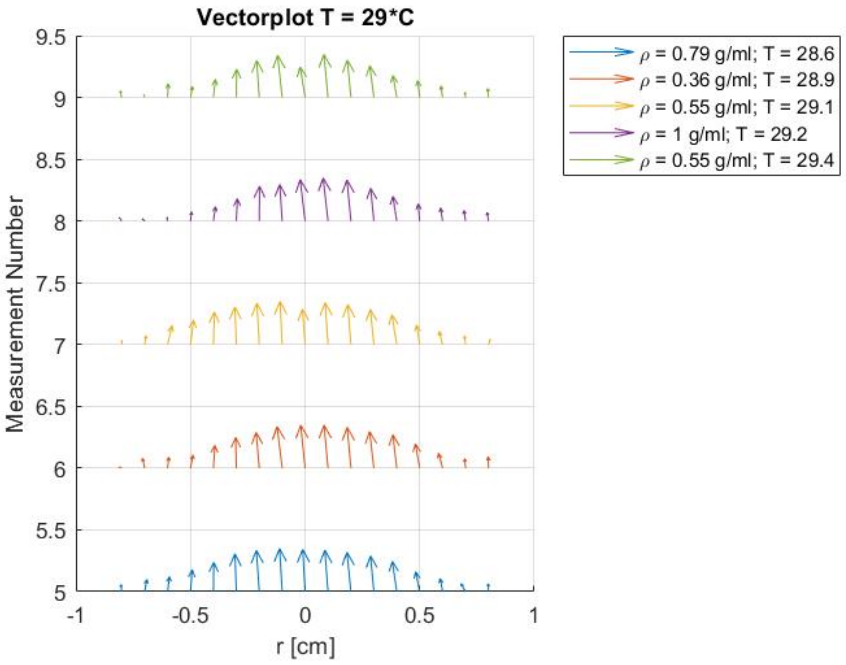

b)

Figure 5.10: Vectorplots of the velocity in the r-direction of the measurements with the inlet temperature in the 27°C and 29°C range. The different measurements are plotted above each other, therefore the vertical dimension has no purpose. The length of the vectors are for comparison only and not for absolute length. The absolute velocities can be found in figures 5.2 and 5.3 for the vertical velocity and figure 5.8.(a and b) for the horizontal velocities.

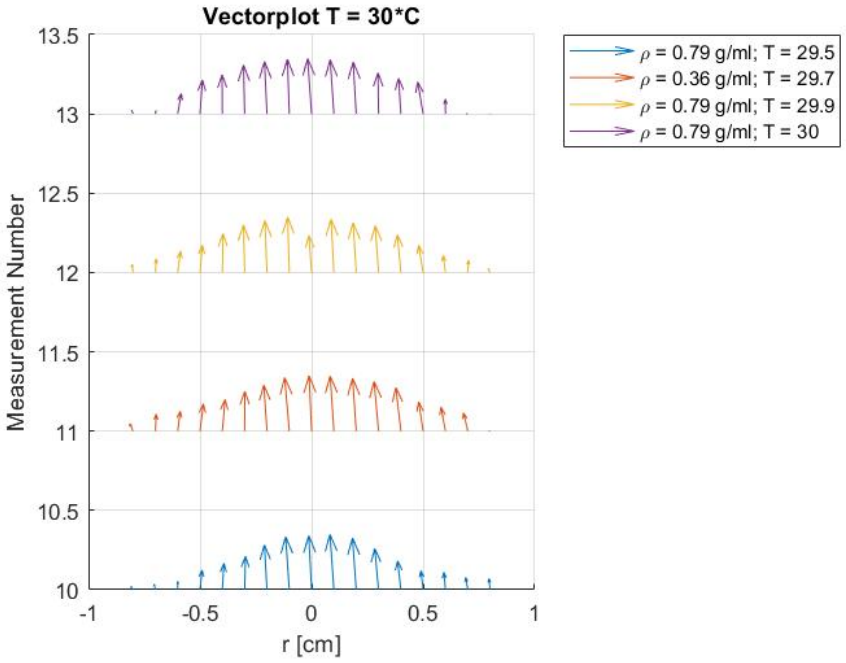

a)

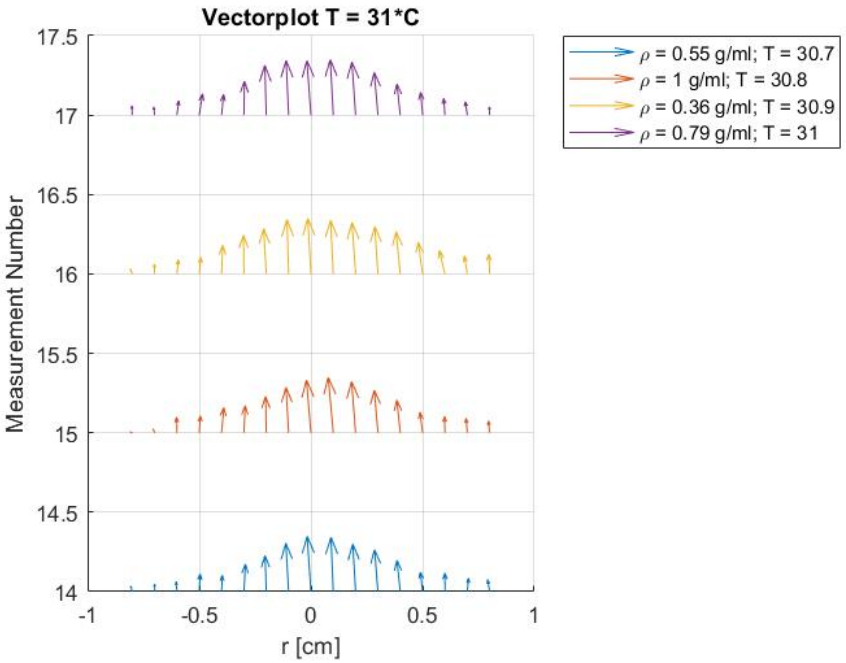

b)

Figure 5.11: Vectorplots of the velocity in the *r*-direction of the measurements with the inlet temperature in the 30°*C* and 31°*C* range. The different measurements are plotted above each other, therefore the vertical dimension has no purpose. The length of the vectors are for comparison only and not for absolute length. The absolute velocities can be found in figures 5.4 and 5.5 for the vertical velocity and figures 5.8.c and 5.9.a for the horizontal velocities.

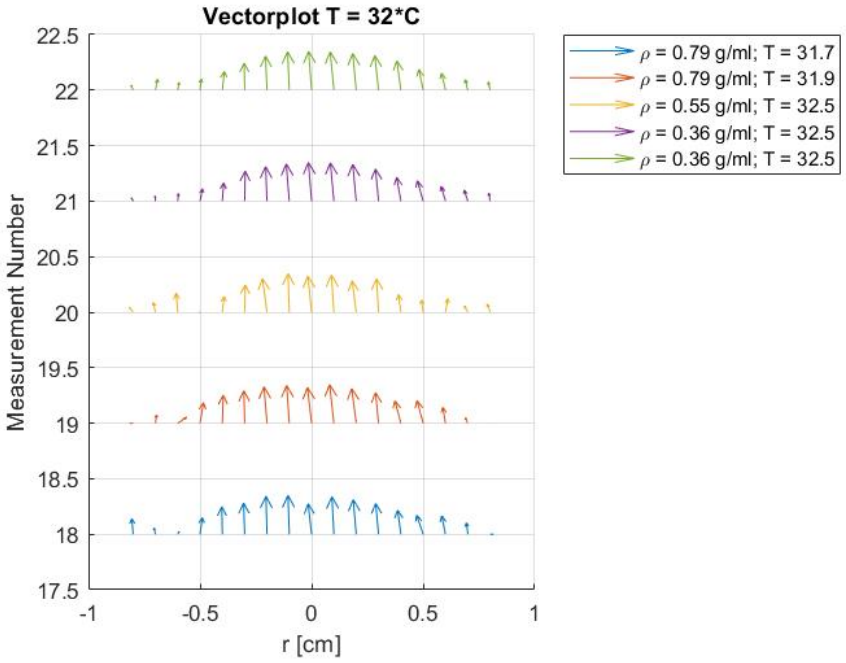

a)

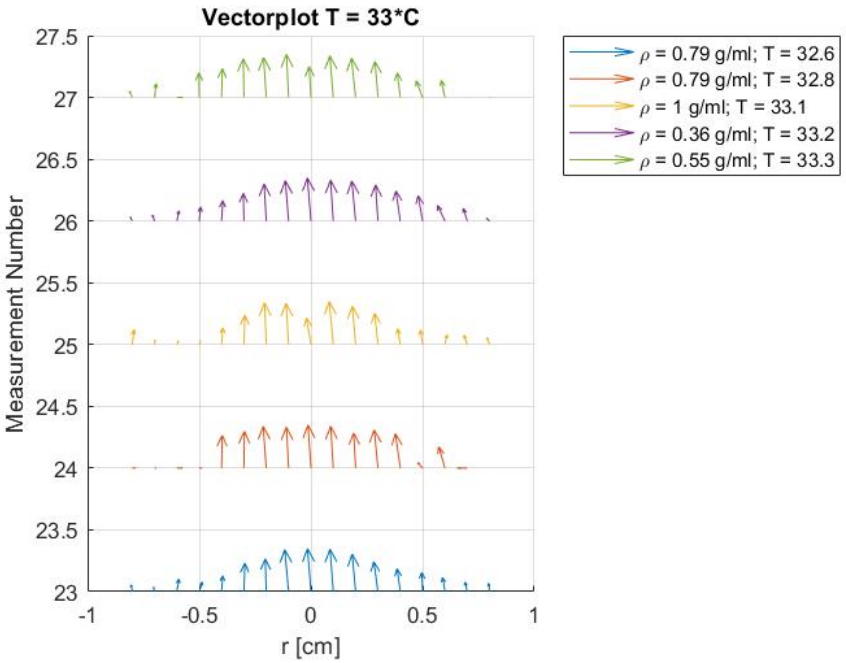

b)

Figure 5.12: Vectorplots of the velocity in the r-direction of the measurements with the inlet temperature in the 32°C and 33°C range. The different measurements are plotted above each other, therefore the vertical dimension has no purpose. The length of the vectors are for comparison only and not for absolute length. The absolute velocities can be found in figures 5.6 and 5.7 for the vertical velocity and figure 5.9.(b and c) for the horizontal velocities.

is expected between the simulations and the experimental data. However, as shown in figure 5.13, the results do not agree with this statement. The simulations show a larger inlet velocity (open symbols) than outlet velocity (cross symbols). This is in contradiction with the experimental results, as these show a larger outlet velocity than inlet velocity in all measurements with an inlet temperature around 27°C. With a density of 0.754 g/ml at 27°C, the seeding with 0.79 g/ml density is expected to show the most accurate results, as the difference in density is the smallest and therefore the slip velocity as well.

The simulated inlet velocity ($u_{in,sim,\ 27°C} = 44.84$ cm/s) is nearly ten times the experimental inlet velocity ($u_{in,\ 27°C} = 4.52$ cm/s) as seen in figure 5.13, blue open symbol. As the inlet interface measurement is done in the center of the jet at $r = y = 0$ mm, the velocity $\overline{u}$ is expected to be around its maximum. The calculated velocity u_s will therefore be a reference for the velocity at the inlet. As said in section 2.3.1, $u_s = 33.7$ cm/s was calculated with variables from the measurements itself and is in more accordance with the simulations than the experimental results. But apart from the simulated results, the experimental measurements show some accordance among themselves. The two measurements with the 0.79 g/ml seeding (figure 5.13, blue and magenta symbols) show great accordance with each other as the confidence intervals overlap significantly. This may indicate a faulty simulation as well.

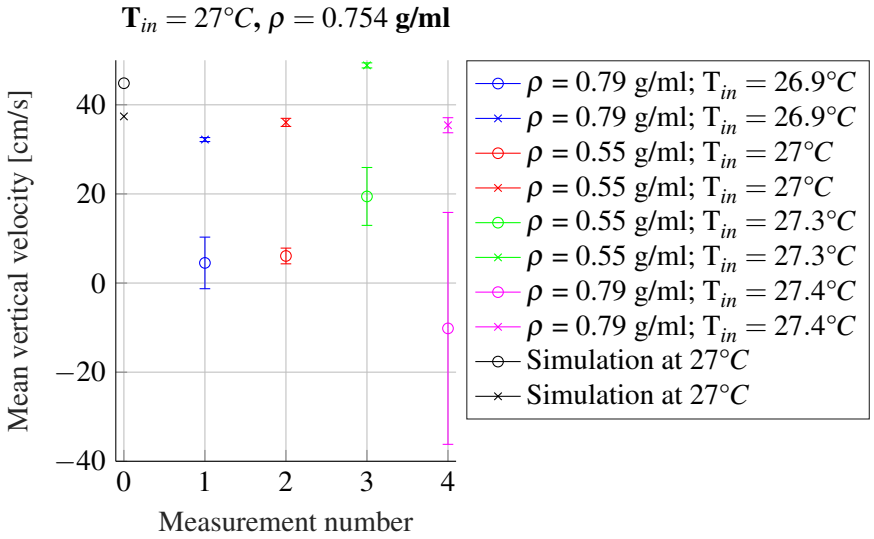

Figure 5.13: Inlet interface and outlet interface measurements done with an inlet temperature around 27°C. The freon density at these conditions is 0.754 g/ml [34]. The inlet velocity of the simulation is $u_s = 33.7$ cm/s, calculated with equation 2.4 with a massflow $\dot{m} = 20 \pm 0.5$ g/s as measured with the Coriolis meter. The open symbols represent the inlet interface and the cross symbols the outlet interface.

When surpassing the critical temperature, the accordance drops significantly. As shown in figures 5.14 and 5.15, the simulated velocities show little agreement with the experimental results. Among the results themselves little agreement can be seen as well, because the different seeding types give unsimilar results. However, both 29°C inlet temperature with 0.55 g/ml seeding cases show resemblance, which indicates that the flow shows similar results for measurements with the same seeding type, even though the measurements were done at different days. The resemblance is gone at the 30°C inlet temperature case as measurements of the same seeding type result in totally different velocities. These discrepancies can be a result of the heavily shifting properties of the

freon around the pseudo-critical point, which creates greatly different conditions for the 29.5°C, 29.9°C and 30.0°C measurements (figure 5.15; blue, red and magenta symbols, respectively).

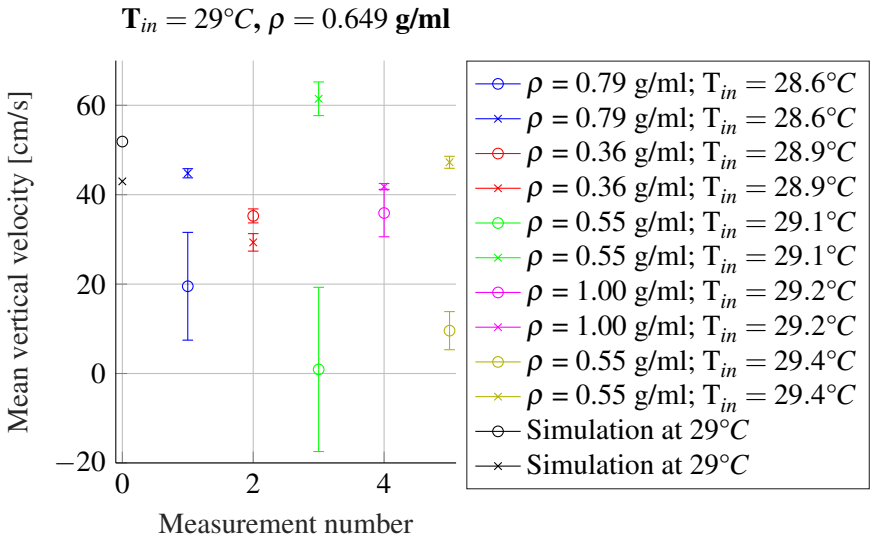

Figure 5.14: Inlet interface and outlet interface measurements done with an inlet temperature around 29°C. The freon density at these conditions is 0.649 g/ml [34]. The inlet velocity of the simulation is $u_s = 39.2$ cm/s, calculated with equation 2.4 with a massflow $\dot{m} = 20 \pm 0.5$ g/s as measured with the Coriolis meter. The open symbols represent the inlet interface and the cross symbols the outlet interface.

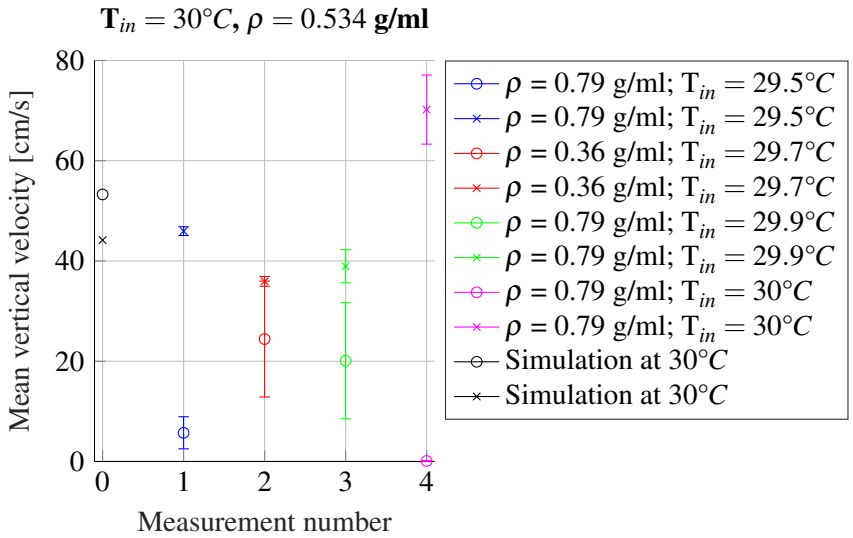

Figure 5.15: Inlet interface and outlet interface measurements done with an inlet temperature around 30°C. The freon density at these conditions is 0.534 g/ml [34]. The inlet velocity of the simulation is $u_s = 47.7$ cm/s, calculated with equation 2.4 with a massflow $\dot{m} = 20 \pm 0.5$ g/s as measured with the Coriolis meter. The open symbols represent the inlet interface and the cross symbols the outlet interface.

Further above the critical temperature, in the $T_{in} = 31°C$ case, the similarities return. Almost all seeding types result in the same outlet velocity around 46.5 ± 1 cm/s. The inlet velocity, with

larger confidence intervals, have the same agreement between the different measurements. Only the simulated velocities and the 0.79 g/ml seeding measurement (magenta line in figure 5.16) show no similarity with the other measurements. The difference can be explained by the large slip velocity due the the density difference between the seeding particles and the freon at $T_{in} = 31°C$. However, the 1.00 g/ml seeding type shows great accordance with an even larger density difference.

In the $32°C$ case in figure 5.17, the results show more similarity with the simulations. The $31.7°C$ and $31.9°C$ measurements show agreement as these measurements were taken at different days, with different starting conditions, but show similar results. The 0.36 g/ml seeding measurements show less agreement, but the magenta symbols in figure 5.17 show great agreement with the simulation. Since the results are inconsistent, the agreement with the simulation must be seen as a single event, as the other measurement with the 0.36 g/ml seeding type has a 20% decrease in velocity amplitude.

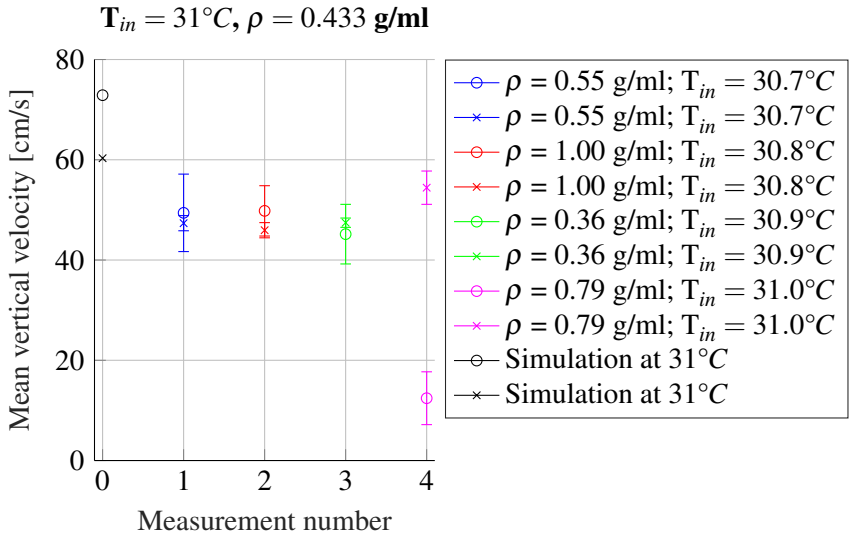

Figure 5.16: Inlet interface and outlet interface measurements done with an inlet temperature around $31°C$. The freon density at these conditions is 0.433 g/ml [34]. The inlet velocity of the simulation is $u_s = 58.8$ cm/s, calculated with equation 2.4 with a massflow $\dot{m} = 20 \pm 0.5$ g/s as measured with the Coriolis meter. The open symbols represent the inlet interface and the cross symbols the outlet interface.

In the $33°C$ case in figure 5.18, the differences in seeding types are clear. The 1.00 g/ml density and 0.79 g/ml density seeding types show no agreement with the simulations at the inlet interface. A non-positive center velocity would mean the freon flows downwards the inlettube and counterclockwise through the tube. This contradicts the velocity calculated from the Coriolis meter at $u_s = 72.3$ cm/s, which flows clockwise because the Coriolis meter is unable to measure the massflow in the opposite direction. Even though the fluid properties might be slightly different than their theoretical counterparts, the fluid cannot flow continuously against eachother. Therefore the blue, red and green symbols in figure 5.18 can be regarded as unrealistic. Many zero velocity reflections surrounding the velocity peak could cause the mean velocity to decrease to zero. The 0.36 g/ml and 0.55 g/ml density seeding types show better agreement at the outlet velocities. This is because the simulated outlet velocity is just outside the confidence intervals of the 0.55 g/ml measurement, but well within the 0.36 g/ml seeding type measurement: $u_{in,\ 33°C} = 79.06 \pm 2.91$ cm/s with a simulated velocity of $u_{in,sim,\ 33°C} = 81.22$ cm/s.

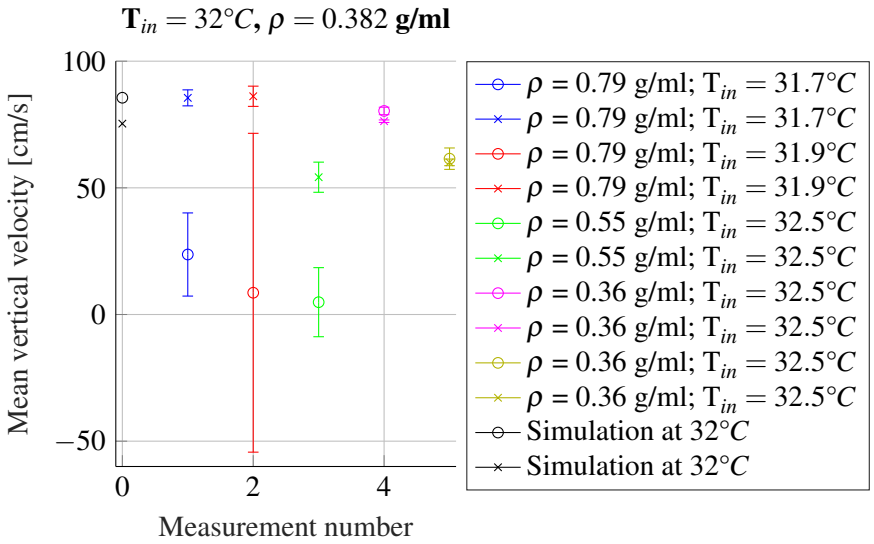

Figure 5.17: Inlet interface and outlet interface measurements done with an inlet temperature around 32°C. The freon density at these conditions is 0.382 g/ml [34]. The inlet velocity of the simulation is $u_s = 66.7$ cm/s, calculated with equation 2.4 with a massflow $\dot{m} = 20 \pm 0.5$ g/s as measured with the Coriolis meter. The open symbols represent the inlet interface and the cross symbols the outlet interface.

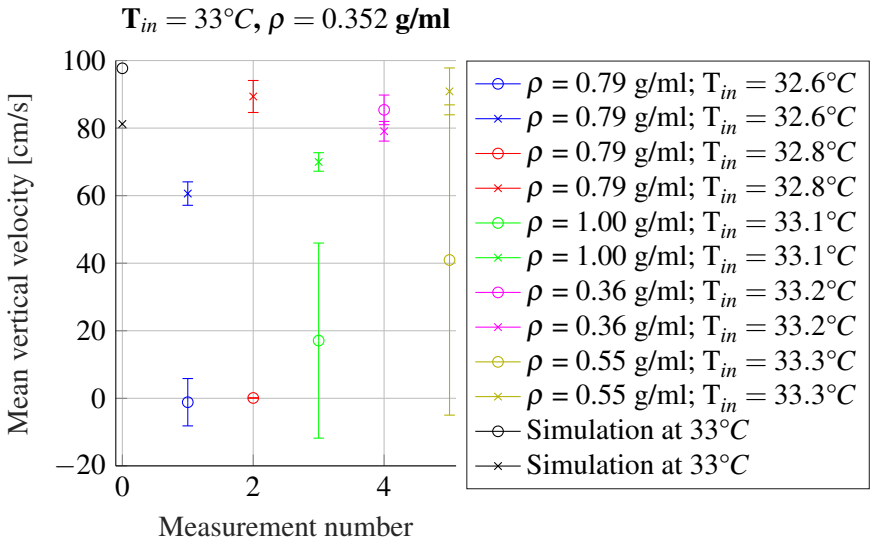

Figure 5.18: Inlet interface and outlet interface measurements done with an inlet temperature around 33°C. The freon density at these conditions is 0.352 g/ml [34]. The inlet velocity of the simulation is $u_s = 72.3$ cm/s, calculated with equation 2.4 with a massflow $\dot{m} = 20 \pm 0.5$ g/s as measured with the Coriolis meter. The open symbols represent the inlet interface and the cross symbols the outlet interface.

5.4 Results Depth-line

The last line of interest is the center depth line, which is located at $r = x = 0$ mm and stretches from $y = -12.5$ mm at the copper backside to $y = 12.5$ mm at the front glass window.

Similar to the centerline, the similarity between the depth-line experimental results and the sim-

ulations are low. The simulations show a much lower amplitude than the experimental results, which is signified by the multiplier plots in figure 5.19. Even at the higher temperatures where the inlet/outlet interfaces showed better agreement, the amplitude of the experimental results is three times higher than the simulated results. The different seeding types all show great agreement with each other, as they all exhibit a similar velocity profile.

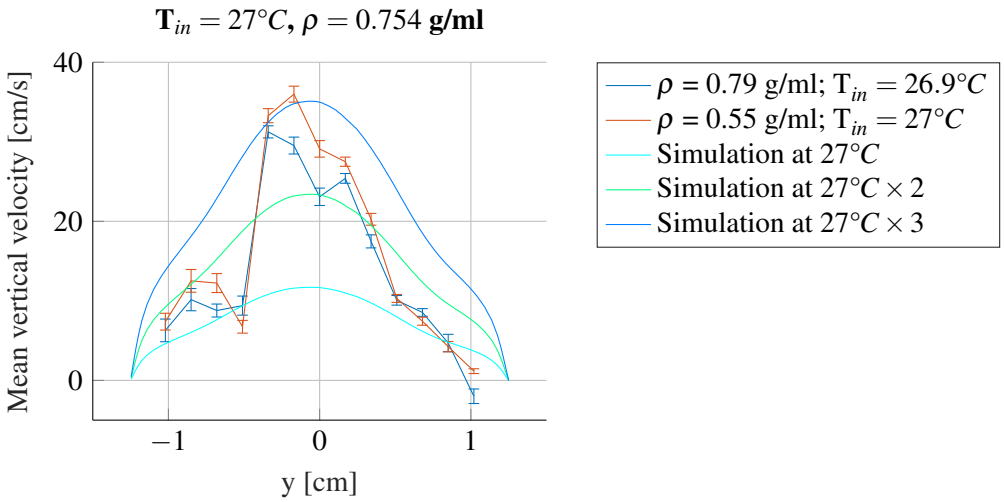

Figure 5.19: Depthline measurements done with an inlet temperature around 27°C. The freon density at these conditions is 0.754 g/ml [34]. The inlet velocity of the simulation is $u_s = 33.7$ cm/s, calculated with equation 2.4 with a massflow $\dot{m} = 20 \pm 0.5$ g/s as measured with the Coriolis meter.

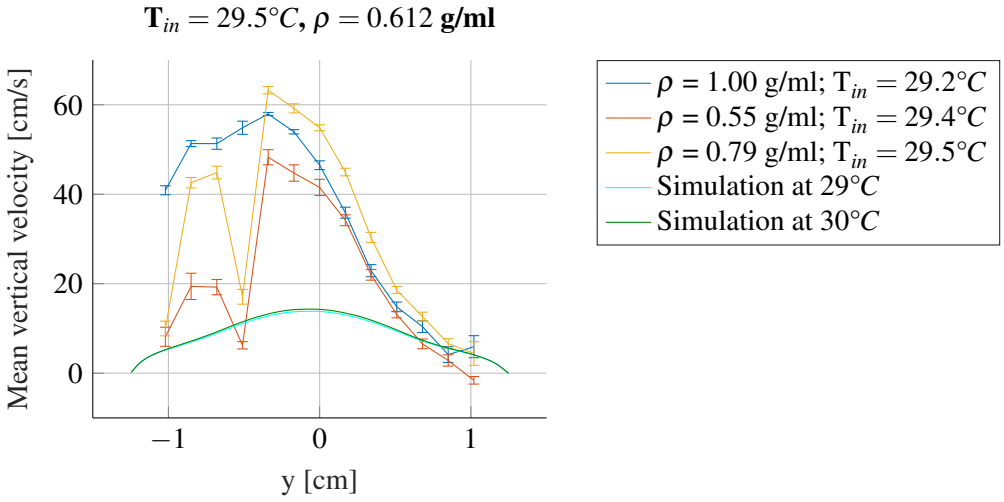

Figure 5.20: Depthline measurements done with an inlet temperature between 29°C and 30°C. The freon density at these conditions are 0.649 g/ml to 0.534 g/ml [34]. The inlet velocity of the simulation is between $u_s = 39.2$ cm/s and 47.7 cm/s, calculated with equation 2.4 with a massflow $\dot{m} = 20 \pm 0.5$ g/s as measured with the Coriolis meter.

An interesting event is the sudden decrease around $y = -0.5$ mm in almost all cases. There is no explanation found in the simulations for this drop. Figure 5.20 and 5.21 show two cases where the drop is not present. These cases both used the 1.00 g/ml seeding type, which in turn could explain the absence of the decrease. This might be because the seeding particles are too heavy and they

overshoot the flow of the fluid, meaning they cannot respond to a sudden drop in velocity. However, in figure 5.22, the 1.00 g/ml seeding density is present as well and shows great agreement with the other seeding particles. A recirculation cannot explain the decrease as a negative mean velocity would be needed for the flow to create a vortex. The structure of the geometry could be created by an unknown vortex from the third unmeasurerable dimension. However, no explicit explanation is found in literature.

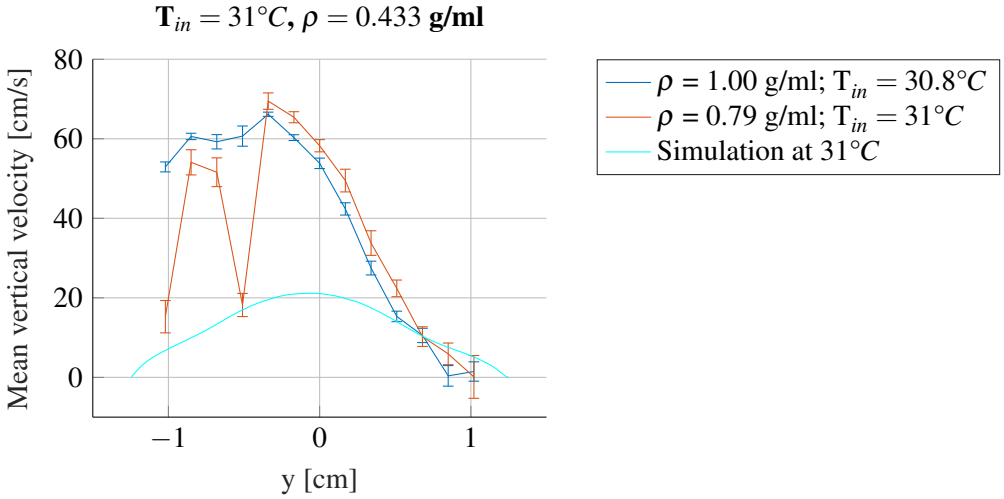

Figure 5.21: Depthline measurements done with an inlet temperature around 31°C. The freon density at these conditions is 0.433 g/ml [34]. The inlet velocity of the simulation is $u_s = 58.8$ cm/s, calculated with equation 2.4 with a massflow $\dot{m} = 20 \pm 0.5$ g/s as measured with the Coriolis meter.

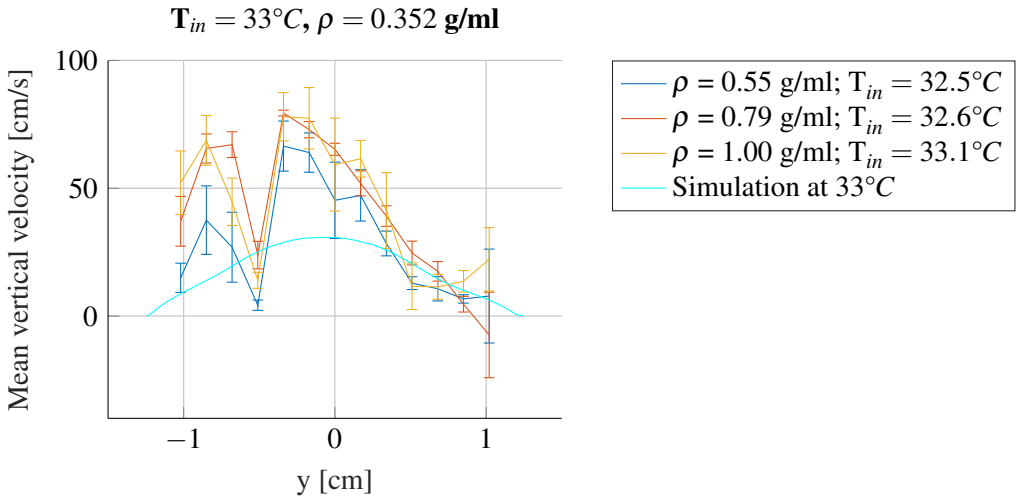

Figure 5.22: Depthline measurements done with an inlet temperature around 33°C. The freon density at these conditions is 0.352 g/ml [34]. The inlet velocity of the simulation is $u_s = 72.3$ cm/s, calculated with equation 2.4 with a massflow $\dot{m} = 20 \pm 0.5$ g/s as measured with the Coriolis meter.

5.5 Local Heating Measurements

The second part of this study is to indicate the feasibility of LDA in a changing density environment. By continuously heating a certain part of the setup, a density difference is applied. This is done via

the copper backside of the measurement volume. The copper backside has three thermocouples and a heating element embedded in it as shown in figure 5.23. Two temperature case experiments were performed at inlet temperatures $T_{in} = 29°C$ and $T_{in} = 31°C$. Both cases consist of one measurement without additional heating and two measurements with different heating power applied. The power supply system of the copper backside has three thermocouples embedded of which one thermocouple (T6) is embedded in the power supply system. The T6 thermocouple marks the temperature of the copper backside, which will be denoted as T_L for Local Temperature.

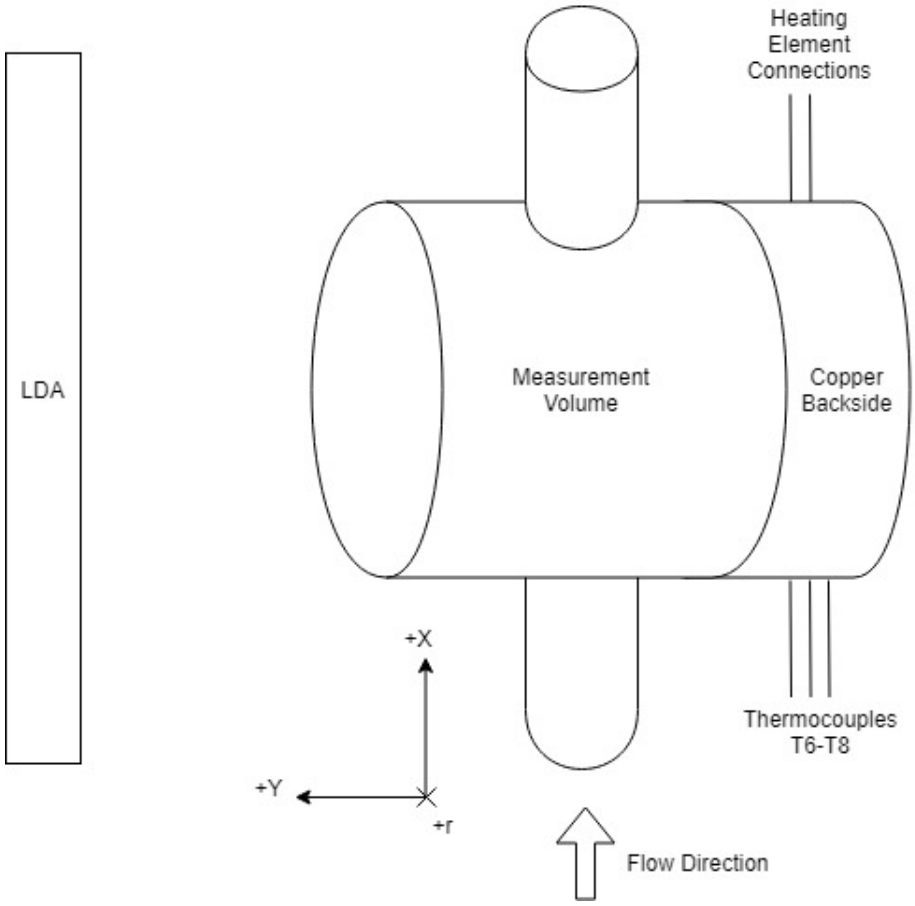

Figure 5.23: The measurement volume viewed from the positive *r*-direction. The copper backside is present with three thermocouples (T6-T8) and the heating element embedded in it. The heating element heats the copper, which transfers the heat to the freon inside the measurement volume.

As with the seeding measurements in previous sections, the pressure was held constant and the inlet temperature was adjusted to keep the pressure constant. The local heating element affected this settings and therefore the inlet temperature is slightly different per measurement. To indicate only the effect of the local heating differences, thetype of seeding to measure the velocity was kept constant throughout all measurements in this section. The seeding type with 0.55 g/ml density was chosen based on the least slip velocity due to density differences with the freon.
As shown in figure 5.24.a, the $29°C$ case shows similar results for all local variations. Significant similarity is shown in the negative *r*-direction as the velocity differences are near zero. The similarity indicates a near zero difference between $\rho_{f;\ T_{in}=29°C,\ blue} - \rho_p$, $\rho_{f;\ T_{in}=29°C,\ red} - \rho_p$ and $\rho_{f;\ T_{in}=29°C,\ yellow} - \rho_p$ and therefore near zero slip velocity differences. Because the fluid density are near equal, there is a negligible temperature increase. In the jet, however, the different measure-

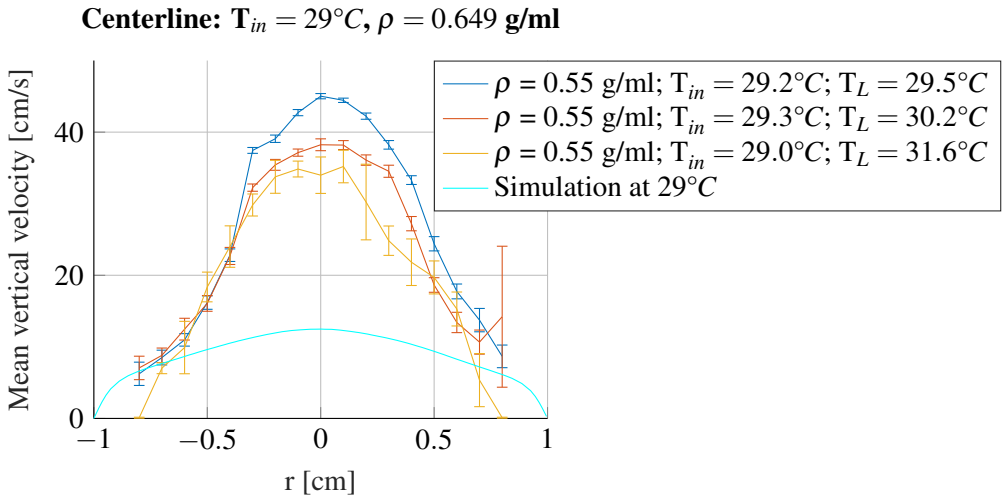

Figure 5.24: Centerline measured at inlet temperatures of 29°C in a) and 31°C in b) with different local temperatures T_L.

ments show differences. Since the inlet of the setup was slightly tilted as explained in section 4.1, an asymmetrical property was expected.

The local heating affects the properties of the fluid and therefore the density is shifting within the window. This creates local spots with density differences due to the temperature gradient. The lasers of the LDA therefore change paths due to the refraction index being dependent on the density[1]. The changing refractive index can create differences between the measurements and the actual measured position as the density within the window is not known. Figure 5.25.a shows there is a large difference in velocity profile between the backside (negative y values) compared to the center ($y = 0$ mm) and the frontside (positive y values). The heated backside creates the largest differences which explains the unpredictable behaviour of the yellow line.

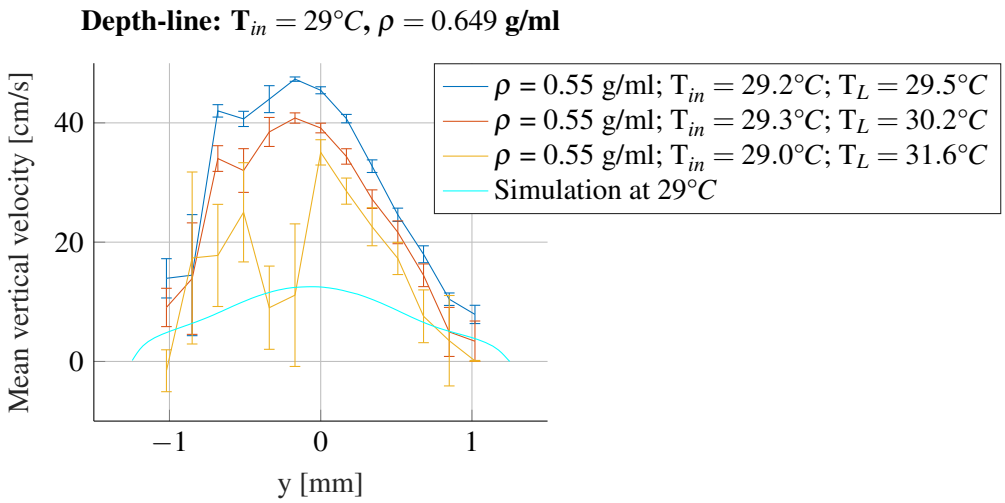

a)

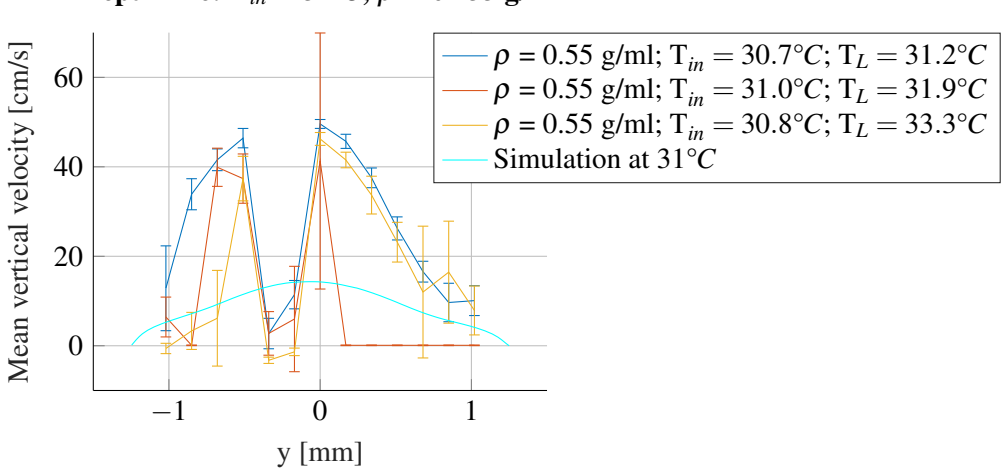

b)

Figure 5.25: Depth-line measured at 29°C in a) and 31°C in b) with local temperature T_L variations.

The yellow line in figure 5.25.a shows a similar profile as the three measurements from the 31°C inlet temperature case in figure 5.25.b. This similarity implies that the sudden decrease in velocity happens above a certain temperature. It appears to be formed when the averaged temperature

[1] This dependency is further elaborated in appendix A.

is increased above the pseudo-critical point at 30°C as this may create very large local density differences. The density differences can therefore create buoyancy effects, which can create local velocity differences. However, these large local density differences can also attribute to large refractive index changes, which affect the velocity measurement creating a misshaped laser intersection volume.

It is believed that the data of the red line in the positive y-range in figure 5.25.b is caused by bad data and many zero velocity reflections.

5.6 Final Considerations

Experimental physics is prone to faulty equipment and failed programs. This study survived a few. The processor processing the reflected signals and converting them to counts, was broken and had to be sent back to Dantec Dynamics [48] in Denmark for over seven weeks. The first cooling installation coupled to the RID building showed effects of the other macheriny in the building using the same cooling installation. A periodic signal was discovered in the pressure data which rendered several measurements unusable due to unstable conditions. The updated secondary cooling system was disconnected from the RID building and served a more stable pressure condition. This resulted in more stable measurement conditions and therefore more accurate measurements.

The temperature fluctuated sometimes as the setup was thought to be at constant condition, but still returned an increased temperature after returning for the data. This might be due to the room being badly ventilated and therefore heating up to 31°C at peak moments. This room temperature affected the setup as well and heated it at extra points thoughout the whole loop. This extra heating could have affected the measurement conditions and therefore the measurements. The heating could also have influenced the equipment, which might result in the data being recorded differently. The BSA flow software [38], which accumulated and could modify the incoming LDA data, crashed several times, rendering the data corrupted or missing. This way, a lot of measurements had to be (partly) redone.

Modification of the LDA parameters could have influenced the data. A different laser power would have given more reflections, but probably also more useless zero reflections. A change in the filters could have the same effect. The maximum number of collectable data samples had an effect on the Excel output. The maximum was set to 500000 at first, however, Excel corrupted the files. Therefore the maximum was set to 200000, which Excel was able to handle. Fulvio Bertocchi helped with setting these parameters to their acceptable situation. More data points could create better confidence intervals and more accurate results.

The simulations were done in Fluent [11]. Several simulations crashed as the shifts between properties were too large to handle or resulted in simulations with unrealistic high velocities (>100 times the experimental results). After help from Yan Zheng, the simulations returned realistic results, which were presented. However, as the accurateness of the simulations is debatable, a different program might have resulted in more accurate simulations.

6. Conclusion

Droplet ©ProMinent [49]

Although feasability studies have been carried out on seeding particles for some years, none were done on supercritical fluids using Laser Doppler Anemometry. Countless types of seeding particles can be made by varying properties of particles like the size of the particle, the material, the density, etc. This study focused on different densities of the particles, namely patricles with density of 1 g/ml, 0.79 g/ml, 0.55 g/ml and 0.36 g/ml. The rest of the properties were kept as constant as possible.

As concluded by Mei (1996) [44], the particle and fluid density ratio shows a good response between 0.56 and 1.62. This way, the 1.00 g/ml seeding type should give acceptable results in the $27°C$ ($\rho_{freon} = 0.754$ g/ml) and the $29°C$ ($\rho_{freon} = 0.649$ g/ml) inlet temperature cases as the density of the fluid falls within the ratio range. Section 5.2 showed that the simulations had little agreement with the experimental results. The shape of the velocity profile and especially the amplitude were unsimilar. The subcritical case at $T_{in} = 27°C$ showed no correspondence between the simulated velocities and the experimental results. An asymmetrical result for the 1.00 g/ml seeding type was found in the $T_{in} = 29°C$ case and shows no similarity to the simulation as well due to the asymmetric profile and the amplitude of the vertical velocities. It falls just within the density ratio at $\rho_p/\rho_f = 1.54$. The 1.00 g/ml seeding type was used in higher temperature measurements for comparison and to see the effects of a heavier seeding particle compared to the seeding particles with less different densities. The 1.00 g/ml overshoots the fluid in the $T_{in} = 33°C$ case as expected due to the density differences. Unexpected behaviour happens in the edge regions, which is expected as the density ratio is 2.84, well above the proposed range.

The range of fluid densities of the 0.79 g/ml seeding density type is between 0.491-1.41 g/ml, which is to the $T_{in} = 30°C$ cases. The $T_{in} = 27°C$ case has two measurements with the 0.79 g/ml seeding type. These measurement do not agree with eachother. The $T_{in} = 29°C$ measurement of 0.55 g/ml has a smooth curve across the centerline, but is about three times the amplitude of the simulated case. The $T_{in} = 30°C$ has three 0.79 g/ml seeding measurements, which are not in agreement with eachother, with one measurement featuring an M-shaped profile, while the remaining measurements do not have this dip. The higher temperature measurements have the same lack of agreement, except for the unique event at $T_{in} = 32°C$, as shown in figure 5.6, where the two measurements are in total agreement at the centerline and both the inlet interface and the outlet interface.

The case at $T_{in} = 29°C$ has two measurements using the 0.55 g/ml seeding type, which measured the same M-shaped velocity profile, but with an averaged 16.5 cm/s difference in the velocity amplitude. The two measurements fromt the $T_{in} = 27°C$ case also show no agreement in the centerline, both interfaces and the depth-line. At $30-33°C$ inlet temperature the single measurements per case show no agreement with the simulation. The agreeable ratio from Mei's study (1996) [44] allows the 0.55 g/ml seeding type to function within 0.982-0.342 g/ml freon density, which

corresponds to the full temperature range up to $T_{in} = 33°C$. The experimental results, however, do not agree to this statement.

The final tested seeding particle is the 0.36 g/ml seeding density particle. This particle showed some correspondence with the $T_{in} = 29°C$ free jet approach, but failed to indicate any agreements up to $T_{in} = 31°C$. In the $T_{in} = 32°C$ case, the particle showed little agreement between the two measurements succesfully done with this particle. The 0.36 g/ml density seeding particle falls within the density ratio with freon densities up to 0.625 g/ml, which is just above freon at $29°C$.

The local heating measurement resulted in an asymmetrical centerline with differences between the measurements. Furthermore, a local velocity amplitude decrease in the depth-line at certain temperatures was found. The velocity amplitude decrease can be a product from the local heating around the pseudo-critical point, which results in large density differences between the front of the measurement volume and the back. As the confidence intervals of the y values in this decrease are large compared to the actual value ($\sim 10.8 \pm 8$ cm/s for the yellow line in figure 5.25.a), there were not many velocity values measured or there were many outliers. Either way, no accurate measurements could be done in the decreased velocity amplitude region. However, it must be noted that the measurements in figure 5.25.b with both the inlet temperature and the local copper backside temperature above the pseudo-critical temperature also resulted in this velocity amplitude decrease. The decrease can still be a result from the density difference as the difference is still 32%. Therefore, Laser Doppler Anemometry is unlikely to be useful in supercritical fluids with large density differences within the measurement volume.

Overall, the particles performed not well in the experimental conditions, as the measurements with the same particles on the same inlet temperature were different and all seeding particles showed little agreement with the simulations. As this might be due to compromised simulations of faulty measurements, as mentioned in section 5.2, the experimental results in that case still have to be in agreement with each other. As this is not the result, Laser Doppler Anemometry is not likely to be used for velocity measurement in supercritical conditions.

Future Study

For future studies it is recommended to look at better simulations of the measurement volume. A finer mesh may give more accurate results. Moreover, a more thermally insulated test loop may decrease heat flux leaks and therefore create a more stable inlet temperature and flow. To study the effects on supercritical fluids better, a less complex geometry is advised. A similar cylinder can be used, but with a length smaller than the radius, $L < r$. This will likely create vortices in only one dimension instead of three dimensional flows as in this study. The flow will then likely be better known and therefore the experimental results can be checked more accurately. The mentioned structure observed in the local heating measurements in section 5.5 suggested a change in the profile around the pseudo-critical temperature. This (sudden) change is not known and can be a subject for further studies.

Table 6.1: Table showing an overview of the results. The result is based more upon the similarity of the velocity profile of the measurement than the amplitude of the velocity profile. The scale stretches from - - (bad similarity) to ++ (good similarity).

T_{in} [$°C$] / Seeding type:	1.00 g/ml	0.79 g/ml	0.55 g/ml	0.36 g/ml
26.9		+		
27.0			+/-	
27.3			- -	
27.4		-		
28.6		+		
28.9				++
29.1			-	
29.2	+/-			
29.4			+/-	
29.5		+/-		
29.7				+
29.9		-		
30.0		- -		
30.7			+/-	
30.8	-			
30.9				+/-
31.0		-		
31.7		-		
31.9		- -		
32.5			+	+ and +/-
32.6		+		
32.8		- -		
33.1	+/-			
33.2				+
33.3			-	

Bibliography

[1] Jeremy Licht, Mark Anderson, and Michael Corradini. “Heat transfer to water at supercritical pressures in a circular and square annular flow geometry”. In: *International Journal of Heat and Fluid Flow* 29.1 (2008), pages 156–166 (cited on page 1).

[2] IL Pioro and RB Duffey. “Heat transfer and gidraulic resistance at supercritical pressures in power-engineering applications, ACME”. In: *New York* (2006) (cited on pages 1, 6).

[3] Ronald J Adrian. “Particle-imaging techniques for experimental fluid mechanics”. In: *Annual review of fluid mechanics* 23.1 (1991), pages 261–304 (cited on page 1).

[4] H Teager. “Some observations on oral air flow during phonation”. In: *IEEE Transactions on Acoustics, Speech, and Signal Processing* 28.5 (1980), pages 599–601 (cited on page 1).

[5] Niels G Deen, Bjørn H Hjertager, and Tron Solberg. “Comparison of PIV and LDA measurement methods applied to the gas-liquid flow in a bubble column”. In: *10th international symposium on applications of laser techniques to fluid mechanics*. 2000 (cited on page 1).

[6] V. Valori. “Rayleigh-Bénard convection of a supercritical fluid: PIV and heat transfer study”. PhD thesis. Delft University of Technology, 2018 (cited on pages 1, 23).

[7] John Derek Jackson. “Studies of buoyancy-influenced turbulent flow and heat transfer in vertical passages”. In: *International Heat Transfer Conference 13*. Begel House Inc. 2006 (cited on page 1).

[8] F. Scarano. *Experimental Aerodynamics*. Delft University of Technology, Aerospace Engineering Department – Aerodynamics Section, Feb. 2013 (cited on pages 1, 8–11, 13).

[9] A Melling. “Tracer particles and seeding for particle image velocimetry”. In: *Measurement Science and Technology* 8.12 (1997), page 1406 (cited on page 1).

[10] T Zhang, D Celik, and SW Van Sciver. “Tracer particles for application to PIV studies of liquid helium”. In: *Journal of low temperature physics* 134.3-4 (2004), pages 985–1000 (cited on page 1).

[11] *FLUENT Release 18.1*. ANSYS, Inc. (cited on pages 2, 27, 53).

[12] Ice River Springs. *Bubbles and Waves*. URL: `https://iceriversprings.com/bubbles-and-waves/` (cited on page 3).

[13] nuclear-power.net. *Critical Point of Water*. URL: `https://www.nuclear-power.net/nuclear-engineering/materials-nuclear-engineering/properties-of-water/critical-point-of-water/` (cited on page 3).

[14] lazysupply.co. *Refrigerant Phase Diagram*. URL: `http://lazysupply.co/refrigerant-phase-diagram.html` (cited on page 4).

[15] Steven A Benner, Alonso Ricardo, and Matthew A Carrigan. "Is there a common chemical model for life in the universe?" In: *Current opinion in chemical biology* 8.6 (2004), pages 672–689 (cited on page 4).

[16] Kiana Samadzadeh Chemistry LibreTexts. *Supercritical Fluids*. June 2019. URL: https://chem.libretexts.org/Bookshelves/Physical_and_Theoretical_Chemistry_Textbook_Maps/Supplemental_Modules_(Physical_and_Theoretical_Chemistry)/Physical_Properties_of_Matter/States_of_Matter/Supercritical_Fluids (cited on page 4).

[17] MathWorks. *MATLAB r2017b*. 2017 (cited on page 5).

[18] Ian H. Bell et al. "Pure and Pseudo-pure Fluid Thermophysical Property Evaluation and the Open-Source Thermophysical Property Library CoolProp". In: *Industrial & Engineering Chemistry Research* 53.6 (2014), pages 2498–2508. DOI: 10.1021/ie4033999. eprint: http://pubs.acs.org/doi/pdf/10.1021/ie4033999. URL: http://pubs.acs.org/doi/abs/10.1021/ie4033999 (cited on pages 5, 7).

[19] M. Corradini J. Licht M. Anderson. "Heat Transfer and Fluid Flow Characteristics in Supercritical Pressure Water". In: (2009) (cited on pages 6, 18).

[20] JD Jackson. "Influences of buoyancy on heat transfer to fluids flowing in vertical tubes under turbulent conditions". In: *Turbulent forced convection in channels and bundles* 2 (1979), pages 613–640 (cited on pages 6, 18).

[21] VA Kurganov, Yu A Zeigarnik, and IV Maslakova. "Heat transfer and hydraulic resistance of supercritical-pressure coolants. Part I: Specifics of thermophysical properties of supercritical pressure fluids and turbulent heat transfer under heating conditions in round tubes (state of the art)". In: *International Journal of Heat and Mass Transfer* 55.11-12 (2012), pages 3061–3075 (cited on page 6).

[22] JD Jackson. "Forced convection heat transfer to fluids at supercritical pressure". In: *Turbulent forced convection in channels and bundles* 2 (1979), page 563 (cited on page 6).

[23] Kyoung W Seo. "Heat Transfer Mechanism in Supercritical Fluids: Analysis and Model Developments". PhD thesis. Ph. D. thesis, Pohang University, Pohang, 2005 (cited on page 6).

[24] JD Jackson. "Some striking features of heat transfer with fluids at pressures and temperatures near the critical point". In: *Keynote Paper for International Conference on Energy Conversion and Application (ICECA '2001), Wuhan, China*. 2001 (cited on page 6).

[25] Wikipedia. *Trihalomethane*. Jan. 2019. URL: https://en.wikipedia.org/wiki/Trihalomethane (cited on page 6).

[26] J. Andrew Schoen. *refchart*. 2009. URL: https://web.archive.org/web/20090319184345/http://www.jandrewschoen.com:80/refchart.pdf (cited on pages 6, 15).

[27] ShivaKumar Kyasa. "Fluoroform (CHF3)". In: *Synlett* 26.13 (2015), pages 1911–1912 (cited on page 6).

[28] Wikipedia. *Fluoroform*. July 2019. URL: https://en.wikipedia.org/wiki/Fluoroform (cited on page 6).

[29] S. Mokry I. Pioro. "Thermophysical Properties at Critical and Supercritical Conditions". In: (2011) (cited on page 6).

[30] Frans TM Nieuwstadt, Jerry Westerweel, and Bendiks J Boersma. *Turbulence: introduction to theory and applications of turbulent flows*. Springer, 2016 (cited on pages 6, 7).

[31] Hendrik Tennekes, John Leask Lumley, JL Lumley, et al. *A first course in turbulence*. MIT press, 1972 (cited on page 7).

[32] C Fukushima, L Aanen, and Jerry Westerweel. “Investigation of the mixing process in an axisymmetric turbulent jet using PIV and LIF”. In: *Laser techniques for fluid mechanics*. Springer, 2002, pages 339–356 (cited on page 7).

[33] François G Schmitt. “About Boussinesq’s turbulent viscosity hypothesis: historical remarks and a direct evaluation of its validity”. In: *Comptes Rendus Mécanique* 335.9-10 (2007), pages 617–627 (cited on page 7).

[34] Mark O. McLinden ric W. Lemmon and Daniel G. Friend. “Thermophysical Properties of Fluid Systems”. In: 2019. DOI: https://doi.org/10.18434/T4D303 (cited on pages 7, 8, 34–37, 44–49).

[35] BRB. *BRB launches a low viscosity MH silicone fluid for formulators*. 2019. URL: https://www.brb-international.com/news/2017/01/brb-launches-a-low-viscosity-mh-silicone-fluid-for-formulators (cited on page 15).

[36] D.W. de Haas. *Scrooge Measurements 2018*. June 2018 (cited on pages 16, 18, 19, 22).

[37] National Instruments. *LabView* (cited on page 21).

[38] Dantec Dynamics. *BSA Flow Software v5.02*. 2011 (cited on pages 21, 53).

[39] D.W. de Haas. *Laser Measurement Techniques at NERA*. Aug. 2015 (cited on page 22).

[40] Markus Raffel et al. *Particle image velocimetry: a practical guide*. Springer, 2018 (cited on page 23).

[41] Lara Adrian, Ronald J Adrian, and Jerry Westerweel. *Particle image velocimetry*. 30. Cambridge University Press, 2011 (cited on page 24).

[42] Wolgang Merzkirch. *Flow visualization*. Elsevier, 2012 (cited on page 24).

[43] Richard W Johnson. *Handbook of fluid dynamics*. Crc Press, 2016 (cited on page 24).

[44] R Mei. “Velocity fidelity of flow tracer particles”. In: *Experiments in Fluids* 22.1 (1996), pages 1–13 (cited on pages 24, 55).

[45] R. D. Gould L. H. Benedict. “Towards better uncertainty estimates for turbulence statistics”. In: *Experiments in Fluids* 22 (1996), pages 129–136 (cited on pages 25, 68, 69).

[46] J. Petts. *Stream_of_water.jpg*. 2013. URL: https://commons.wikimedia.org/wiki/File:Stream_of_water.jpg (cited on page 27).

[47] Flow Control Network. *KEY CONSIDERATIONS FOR USING BIODEGRADABLE HYDRAULIC FLUID*. 2015. URL: https://www.flowcontrolnetwork.com/key-considerations-for-using-biodegradable-hydraulic-fluid/ (cited on page 33).

[48] Nova Instruments Company. *Dantec Dynamics*. 2019. URL: https://www.dantecdynamics.com/ (cited on page 53).

[49] ProMinent. *Metering of Fluids*. 2019. URL: https://www.prominent.com/en/Applications/Applications/Metering-of-Fluids/Metering-of-Fluids.html (cited on page 55).

[50] JGraph Ltd. *draw.io*. 2019 (cited on page 63).

[51] Mikhail Polyanskiy RefractiveIndex.info. *Refractive Index of Air*. 2019. URL: https://refractiveindex.info/?shelf=other&book=air&page=Ciddor (cited on page 65).

[52] Mikhail Polyanskiy RefractiveIndex.info. *Refractive Index of Glass*. 2019. URL: https://refractiveindex.info/?shelf=3d&book=glass&page=BK7 (cited on page 65).

[53] Maurice H Quenouille et al. “Problems in plane sampling”. In: *The Annals of Mathematical Statistics* 20.3 (1949), pages 355–375 (cited on page 68).

[54] John Tukey. “Bias and confidence in not quite large samples”. In: *Ann. Math. Statist.* 29 (1958), page 614 (cited on page 68).

[55] B Efron. “Bootstrap methods: another look at the jackknife annals of statistics 7: 1–26”. In: *View Article PubMed/NCBI Google Scholar* (1979) (cited on page 68).

[56] Bradley Efron and Robert J Tibshirani. *An introduction to the bootstrap*. CRC press, 1994 (cited on page 68).

A. Traverser System

A.1 Path of the Lasers

The LDA makes use of two sets of two lasers, which penetrate the freon via a glass window. These lasers are refracted when the interfaces between the three different media are met. Therefore the laser will not follow the same trajectory it did before the glass window as behind the window. In figure A.1 a diagram of the expected path of the lasers is shown. The exact location inside the fluid is needed for the measurements. Therefore the change of distance of x_3 is needed as a function of the location of the LDA source with respect to the glass window x_1.

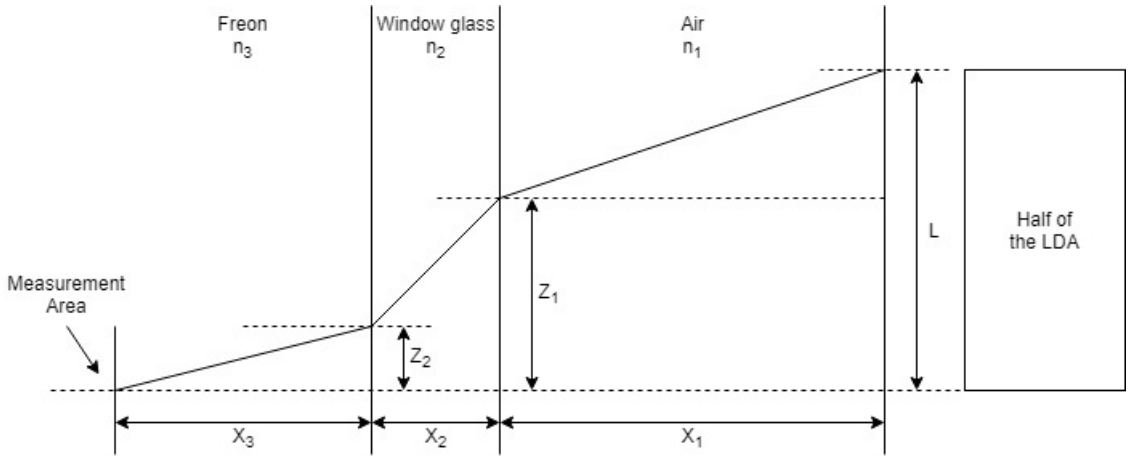

Figure A.1: The trajectory of the lasers from the LDA to the measurement area in the freon. Only one half of a laser pair is presented. n_i stands for the refractive index of the material in that area, x_i the distance between the LDA, measurement area and the material intersections, z_i the height at those intersections and L the length of half the separation between the LDA lasers. Diagram created with draw.io [50].

From figure A.1 the following relationships can be derived using trigonometrical functions.

$$L - z_1 = x_1 \tan(\theta_1) = \sin(\theta_1) * \sqrt{x_1^2 + (L - z_1)^2} \tag{A.1}$$

$$z_1 - z_2 = x_2 \tan(\theta_{2,B}) = \sin(\theta_2) * \sqrt{x_2^2 + (z_1 - z_2)^2} \tag{A.2}$$

$$z_2 = x_3 \tan(\theta_3) = \sin(\theta_3) * \sqrt{x_3^2 + z_2^2} \tag{A.3}$$

The angles are all set as the angle between the laser path and the normal to the interface (the dotted lines). At the interfaces between the different media in figure A.1 Snell's law can be applied. Snell's

law at the two boundaries is written as:

$$n_1 \sin\theta_1 = n_2 \sin\theta_{2,A} \tag{A.4}$$
$$n_2 \sin\theta_{2,B} = n_3 \sin\theta_3 \tag{A.5}$$

Because the angle is the same at both boundaries in the glass window, $\theta_{2,A} = \theta_{2,B} = \theta_2$ and the following expression is valid as well:

$$n_1 \sin\theta_1 = n_3 \sin\theta_3 \tag{A.6}$$

Therefore, equation A.2 and A.3 can be rewritten to:

$$z_1 - z_2 = \frac{n_1}{n_2} \sin(\theta_1) * \sqrt{x_2^2 + (z_1 - z_2)^2} \tag{A.7}$$
$$z_2 = \frac{n_1}{n_3} \sin(\theta_1) * \sqrt{x_3^2 + z_2^2} \tag{A.8}$$

Squaring both sides and reshuffling the terms results in:

$$(L - z_1)^2 = x_1^2 \tan^2\theta_1 \tag{A.9}$$
$$(z_1 - z_2)^2 = x_2^2 \frac{\left(\frac{n_1}{n_2}\sin\theta_1\right)^2}{1 - \left(\frac{n_1}{n_2}\sin\theta_1\right)^2} = x_2^2 Q_2^2 \tag{A.10}$$
$$z_2^2 = x_3^2 \frac{\left(\frac{n_1}{n_3}\sin\theta_1\right)^2}{1 - \left(\frac{n_1}{n_3}\sin\theta_1\right)^2} = x_3^2 Q_3^2 \tag{A.11}$$

Here Q_2^2 and Q_3^2 are used to shorten the notations. By returning to the non-squared variables, a linear system is found:

$$L - z_1 = x_1 \tan\theta_1 \tag{A.12}$$
$$z_1 - z_2 = \pm x_2 Q_2 \tag{A.13}$$
$$z_2 = \pm x_3 Q_3 \tag{A.14}$$

Since the right hand side of equation A.13 and A.14 can get negative due to the refractive index ratios, both the positive and negative solution need to stay.

The separation between the LDA lasers is $2L = 60$ mm with a focal length of $f_{LDA} = 300$ mm. Therefore $\tan\theta_1 = \frac{1}{10}$ and $\sin\theta_1 = \sin(\arctan(\frac{1}{10})) = \frac{1}{\sqrt{101}}$. This will simplify to:

$$L - z_1 = x_1/10 \tag{A.15}$$
$$z_1 - z_2 = \pm x_2 \sqrt{\frac{\left(\frac{n_1}{n_2}\right)^2}{101 - \left(\frac{n_1}{n_2}\right)^2}} \tag{A.16}$$
$$z_2 = \pm x_3 \sqrt{\frac{\left(\frac{n_1}{n_3}\right)^2}{101 - \left(\frac{n_1}{n_3}\right)^2}} \tag{A.17}$$

Since the ratios $\frac{n_1}{n_2}$ and $\frac{n_1}{n_3}$ are not larger than 101, as will be seen in section A.2, the square root sign stays real. Therefore both $z_1 - z_2$ and z_2 itself are positive distances, as both $\pm$ signs should be positive and the negative solution can be discarded. Combining equation A.15 to A.17 results in:

$$\begin{aligned} x_3 &= \frac{1}{Q_3}\left(L - x_1 \tan\theta_1 - x_2 Q_2\right) \\ &= \frac{-\frac{x_1}{10} + L - x_2\sqrt{\frac{\left(\frac{n_1}{n_2}\right)^2}{101-\left(\frac{n_1}{n_2}\right)^2}}}{\sqrt{\frac{\left(\frac{n_1}{n_3}\right)^2}{101-\left(\frac{n_1}{n_3}\right)^2}}} \end{aligned} \tag{A.18}$$

with

$$Q_2 = \frac{n_1}{n_2}\left(101 - \left(\frac{n_1}{n_2}\right)^2\right)^{-\frac{1}{2}} \tag{A.19}$$

$$Q_3 = \frac{n_1}{n_3}\left(101 - \left(\frac{n_1}{n_3}\right)^2\right)^{-\frac{1}{2}} \tag{A.20}$$

and x_3 as an inverse linear function of the distance of the LDA to the window glass x_1. The inverse function makes sense, as x_3 increases as x_1 decreases or the LDA moves closer towards the window. The refractive index of air and glass are $n_1 = 1.00027717$ and $n_2 = 1.5168$, respectively [51, 52], therefore $Q_2 = 0.065761$.

A.2 Refractive index of Freon

The refractive index of freon is calculated with the empirical formula as shown in equation A.21. This formula was created by Peter van der Baan, a former employee of the RID.

$$n = 1 + \frac{1.5\rho}{10000} \tag{A.21}$$

T_{in}	n_3	Q_3
27	1.114	4.1685
29	1.099	4.8223
30	1.083	5.8036
31	1.067	7.2969
32	1.058	8.3999
33	1.053	9.1859

Therefore the scaling factor is -0.15 and is given by:

$$\begin{aligned} n_3 &= Scale \times x_1 + Offset \\ &= \frac{-\tan(\theta_1)}{Q_3} \times x_1 + Offset \end{aligned} \tag{A.22}$$

B. Data Processing Techniques

B.1 Data Filtering

As reflections are a significant portion of the samples, most of the time, they need to be eliminated to see the actual values of the velocities. This is done by filtering the data using an simple inverse band gap filter in MATLAB. After the data of all the experiments was loaded in the loading phase of the script, it was filtered per experiment.

```
% Filter for every location in a measurement.
for a = 1:N(A)

    % Check if files exist via the existing matrix
    if ismember(a,BB{A}) == 1
        continue
    else

    % New variable to create the filtered subset
    c = 1;

    % Circle around every sample value to see if they pass the filter
    for ii = 1:length(V{a}(:,1))

        % Value in V must be above the maximum or below the
        % minimum to be passed on to V_2
        if V{a}(ii,2) < All.Vfilter_min(A,a) || V{a}(ii,2) > All.Vfilter_max(A,a)

            V_2{a}(c,:) = V{a}(ii,:);

            c = c + 1;
        end
    end

    % Calculate wanted variables as part of the Fil-struct
    Fil.S{A}.Vmean(a) = sum(V_2{a}(:,2))/length(V_2{a}(:,2));
    Fil.S{A}.Vrms(a) = sqrt(sum(V_2{a}(:,2).^2)/length(V_2{a}(:,2)));
    Fil.S{A}.DatarateV(a) = length(V_2{a}(:,2))/All.acqtime;
    end
end
```

The variable **a** is the location variable and indicates the location number of that measurement

within experiment **A** with $\mathbf{A} = 1,2,...,M$. Due to differences in the number of locations (**N**) among experiments, **N** is different for values of **A**.

The existing matrix was formed during the loading phase of the script to indicate any missing or corrupted files among the Excel files. The location numbers of the missing files were stored in a vector, which itself was stored in the cell **BB**. If a file is unusable, that location number will be skipped, without breaking the script. The loading phase of the script loaded the data of all the experiments into an organized structure. All the data about a sample was placed in a row in an array containing all the samples of one location measurement of one experiment. The arrays of the locations of a single experiment were stored in a cell within a struct **Unfil** for 'Unfiltered Data'. The data of the other experiments were also stored the same way in a cell en put in the same struct.

The filtered data is used to calculate the mean $\overline{v}$, the rms v_{rms} and the datarate D_v of the data and these are stored in the struct **Fil** for 'Filtered Data' the same way as the unfiltered data. The exact same is done with the u velocity and stored in the same structs. The acquisition time and both filtervalue matrices are stored in the struct **All**, which contains all the data in the script that is not dependent on the experiment. The filtervalue matrices were hand picked, because the reflection peak has a different width in each experiment (depending on **A**) and even differs per location (depending on **a**) within a measurement. The velocity u was filtered and stored the same way as well as the respective calculated values $\overline{u}, u_{rms}$ and D_u.

B.2 Resampling Method

The data from the LDA is obtained in a random sequence of velocity values. To obtain the confidence intervals of these unorganized sets of data, a resampling method is used. The Jackknife method was first proposed by Quenouille (1949) [53] and then redefined by Tukey (1958) [54], who coined the term. However, a more general resampling method was introduced by Efron in 1979 [55] called the Bootstrap. This method served as the main resampling method. The jackknife method was found to be a linear approximation of the Bootstrap method [56]. The jackknife therefore generally creates less accurate results than the bootstrap due to this approximation, but the difference is negligible at larger number.

B.2.1 Jackknife method

Given a data set $x(x_1, x_2, ..., x_N)$ and some statistical estimator $\hat{\theta}$ (like $\overline{u}$ and $\overline{v}$) determined from this original data set x, the jackknife makes use of the N data subsets that leave out one measurement at a time from the original data set giving $i = 1,2,...,N$ new jackknife data sets. The estimator will then be calculated from these new jackknife samples $x_{jack,i}$ to form the jackknife replications $\hat{\theta}_{jack,i}$ for $i = 1,2,...,N$. For example, the variance can be calculated with equation B.1:

$$\mathrm{var}(\hat{\theta})_{jack} = \frac{N-1}{N}\sum_{i=1}^{N}(\hat{\theta}_{jack,i} - \overline{\hat{\theta}_{jack}})^2 \tag{B.1}$$

where

$$\overline{\hat{\theta}_{jack}} = \frac{1}{N}\sum_{i=1}^{N}\hat{\theta}_{jack,i} \tag{B.2}$$

This gives a confidence interval of the estimator $\hat{\theta}$ of 95% within the interval $\hat{\theta} \pm 1.96\sqrt{\mathrm{var}(\hat{\theta})_{jack}}$ [45].

B.2.2 Bootstrap method

The bootstrap method is built partially the same as the jackknife method. However, instead of leaving one sample out, that measurement is randomly replaced with another independent sample from the set, creating B independent bootstrap sample subsets $x_{boot,1}, x_{boot,2}, ..., x_{boot,B}$. The replacement is always drawn from the original set and not a fictive value. Using these bootstrap samples, the bootstrap replication $\hat{\theta}_{boot,i}$ for $i = 1, 2, ..., B$ can be calculated. Just like the jackknife method, the variance via the bootstrap method is calculated via equation B.3.

$$\text{var}(\hat{\theta})_{boot} = \frac{1}{B-1}\sum_{i=1}^{B}(\hat{\theta}_{boot,i} - \overline{\hat{\theta}_{boot}})^2 \tag{B.3}$$

where

$$\overline{\hat{\theta}_{boot}} = \frac{1}{B}\sum_{i=1}^{N}\hat{\theta}_{boot,i} \tag{B.4}$$

The same interval for the confidence interval of the estimator $\hat{\theta}$ of 95% is found via the bootstrap method: $\hat{\theta} \pm 1.96\sqrt{\text{var}(\hat{\theta})_{boot}}$.

B.2.3 Jackknife restructured

The drawback of both methods were the time constraints. The jackknife method generally needs about $N \times N$ calculations for a set of N samples. The bootstrap method needs about $B \times N$ calculations where B is generally around 100. So above $N = 100$ the bootstrap method is most likely faster than the jackknife method especially since the LDA is able to produce 1000+ samples per set on a regular base.

However, in 1996, Benedict and Gould [45] also presented a faster method to use the jackknife method, cutting the amount of calculations needed from N^2 to N. "*This reduction in computation is accomplished by expanding the individual jackknife centralized moment statistics to create a series of summations composed entirely of noncentralized variables.*" An example is the jackknife estimate of the variance for the estimator $\overline{u^2}$. First, the variance per jackknife sample is written as in equation B.5.

$$\hat{\theta}_{jack,i} = \overline{u^2_{jack,i}} = \frac{1}{N-1}\sum_{j=1,j\neq i}^{N}(U_j - \overline{U_{jack,i}})^2 \tag{B.5}$$

Note the summation over $N-1$ as the replications leave one sample out. Equation B.5 will then be rewritten to equation B.6:

$$\overline{u^2_{jack,i}} = \frac{1}{N-1}\left[\sum_{j=1,j\neq i}^{N}U_j^2 - 2\overline{U_{jack,i}}\sum_{j=1,j\neq i}^{N}U_j + (N-1)(\overline{U_{jack,i}})^2\right] \tag{B.6}$$

Using these restructured formulas during the data processing, the computation time can be severely decreased as N calculations take much less time than $100N$ calculations for the bootstrap method. The restructured jackknife method is used to calculate the uncertainties around the wanted estimators of the LDA data. The 95% confidence interval is then calculated with the formula $\hat{\theta} \pm 1.96\sqrt{\text{var}(\hat{\theta})_{jack}}$. These intervals will be plotted in the results as errorbars around the measured value. As there is no difference in the formulas obtained between the positive and negative

uncertainty, the errorbars will be symmetric around the measured value. This value will be the measured velocity in case of the LDA data. It does not matter which velocity is resampled as the resampling method is independent of any direction. Therefore the vertical and horizontal velocity can be resampled independent of each other to gain their uncertainties.

B.2.4 Jackknife code

The jackknife method is done within the same script as was used for the filtering within the same experiment *for*-loop (*for*-loop with $\mathbf{A}= 1,2,...,N$). To minimize the necessary computation power, the intermediate variables are all cleared after they are used per location.

```
for a = 1:N(A)

    Vmeanjackmean = 1/L*sum(Vmeanjack);
    Vjackvar = (L-1)/L*sum((Vmeanjack - Vmeanjackmean)^2);
    V_VAR{A}(a) = 1.96*sqrt(Vjackvar);

end
```

Here **Vmeanjack** is the estimator $\hat{\theta}_{jack,i}$ of the mean velocity $\overline{v}$. These mean values are taken over the N subsets with $N-1$ samples. These N estimators $\hat{\theta}_{jack,i}$ were averaged over N to create $\overline{\hat{\theta}_{jack}}$, which is needed to calculate the variance $\mathrm{var}(\hat{\theta})_{jack}$, with variable **Vjackvar**, and the confidence interval with variable **V_VAR**. This piece of code is executed for wanted every estimator, like $\overline{v}$ (as seen above), $\overline{u}$, v_{rms} and u_{rms}.

C. Inlet/Outlet Table

The inlet and outlet interface measurements in section 5.3 are listed in table C.1. The velocities are shown together with their 95% confidence interval in the row next to them. The confidence intervals are listed as the single length between the measurement and one errorbar.

T_{in}	ρ_{seed}	u_{in}	u_{in} 95%	u_{out}	u_{out} 95%
26.9	0.79	4.52	5.79	32.21	0.45
27	0.55	6.08	1.76	36.06	0.91
27.3	0.55	19.44	6.50	48.85	0.57
27.4	0.79	-10.18	26.02	35.42	1.69
28.6	0.79	19.52	12.05	44.79	1.03
28.9	0.36	35.26	1.57	29.33	1.96
29.1	0.55	0.92	18.37	61.46	3.76
29.2	1.00	35.90	5.30	41.80	0.70
29.4	0.55	9.59	4.27	47.25	1.34
29.5	0.79	5.72	3.20	45.96	0.88
29.7	0.36	24.42	11.56	35.94	0.98
29.9	0.79	20.09	11.58	38.95	3.31
30	0.79	0.10	0.07	70.20	6.89
30.7	0.55	49.41	7.73	47.35	1.51
30.8	1.00	49.81	5.02	45.95	1.52
30.9	0.36	45.16	5.95	47.45	0.93
31	0.79	12.43	5.27	54.43	3.32
31.7	0.79	23.69	16.41	85.52	3.16
31.9	0.79	8.59	62.93	86.15	3.99
32.5	0.55	4.86	13.64	54.20	5.95
32.5	0.36	80.36	1.48	76.31	0.50
32.5	0.36	61.51	4.23	60.05	1.31
32.6	0.79	-1.15	7.01	60.61	3.47
32.8	0.79	0.10	0.07	89.36	4.74
33.1	1.00	17.09	28.88	69.98	2.75
33.2	0.36	85.40	4.39	79.06	2.91
33.3	0.55	40.95	45.93	90.87	6.94

Table C.1: All inlet and outlet interface measurements listed. The 95% confidence interval length is shown in the row next their respective velocity. It is shown as $u_{in} \pm u_{in}95\%$. Measurements also shown in section 5.3 and figures 5.13-5.18.